5-1-2012

A Refreshable and Portable E-Braille System for the Blind and Visually Impaired

Mohammad Yousef Saadeh
University of Nevada, Las Vegas, m.mechat@yahoo.com

Repository Citation

Saadeh, Mohammad Yousef, "A Refreshable and Portable E-Braille System for the Blind and Visually Impaired" (2012). *UNLV Theses, Dissertations, Professional Papers, and Capstones*. 1619.
https://digitalscholarship.unlv.edu/thesesdissertations/1619

A REFRESHABLE AND PORTABLE E-BRAILLE SYSTEM FOR THE BLIND AND VISUALLY IMPAIRED

by

Mohammad Yousef Saadeh

Bachelor of Science
University of Jordan
2005

Master of Science
International Islamic University Malaysia
2007

A dissertation submitted in partial fulfillment
of the requirements for the

Doctor of Philosophy in Mechanical Engineering

Department of Mechanical Engineering
Howard R. Hughes College of Engineering
The Graduate College

University of Nevada, Las Vegas
May 2012

THE GRADUATE COLLEGE

We recommend the dissertation prepared under our supervision by

Mohammad Yousef Saadeh

entitled

A Refreshable and Portable E-Braille System for the Blind and Visually Impaired

be accepted in partial fulfillment of the requirements for the degree of

Doctor of Philosophy in Mechanical Engineering
Department of Mechanical Engineering

Mohamed Trabia, Committee Chair

Woosoon Yim, Committee Member

Brendan O'Toole, Committee Member

Robert Boehm, Committee Member

Gabriele Wulf, Graduate College Representative

Ronald Smith, Ph. D., Vice President for Research and Graduate Studies
and Dean of the Graduate College

May 2012

ABSTRACT

A Refreshable and Portable E-Braille System for the Blind and Visually Impaired

by

Mohammad Yousef Saadeh

Dr. Mohamed B. Trabia, Examination Committee Chair
Professor of Mechanical Engineering
University of Nevada Las Vegas

The objective of this research is to design an affordable Braille tactile display that is wearable, refreshable, and portable. The device is intended to be used as an output device that can playback stored media. It can be also incorporated with current Braille reading technologies. The device will control both the electrical and mechanical stimulations to optimize the sensation and ensure extended use of the device. This work is concerned mainly with the mechanical aspects of the design.

This research proposed the development of a finger-wearable, scanning-style electric-stimulation based (electrotactile) Braille display with sensing and adaptive rendering/actuation functions for assisting the BVI. E-Braille technology will allow the BVI to perform important tasks such as reading, writing, typing in Braille, printing text, browsing the Internet, engaging in on-line conversations, and perceiving graphics. Combined with the Cyber-Infrastructure network technology, E-Braille will allow the BVI to access more text, books and libraries anytime and anywhere. Additionally, the proposed E-Braille will provide a tool for collaborative research in the biomedical field involving psychophysicists, neurocytologists, electrochemists, and cognitive scientists.

E-Braille will fill a gap in portable and adaptive “seeing” rehabilitation technology by providing the BVI with a fast, refreshable, and individualized electronic Braille tactile display. The proposed E-Braille system will dramatically enhance the lives of millions of the BVI by providing them with unprecedented access to information and communication at an affordable price and using the state-of-the-art sensing technology.

TABLE OF CONTENTS

LIST OF TABLES

LIST OF FIGURES

CHAPTER 1

INTRODUCTION

The Braille System

The Braille system, devised in 1821 by Louis Braille, is widely used by the BVI to read and write. The Braille code generally consists of cells of six raised dots arranged in a grid of two dots horizontally by three dots vertically. The dots are conventionally numbered 1, 2, and 3 from the top of the left column and 4, 5, and 6 from the top of the right column, specification of these characters are listed in Appendix I.

A dot may be raised at any of the six positions to form sixty-three (2^6-1) permutations. The presence or absence of dots gives the coding for different symbols. A variety of Braille codes exist, which are used to map character sets of different languages, mathematics, music, and more. Even though the structure of the Braille system remains the same, every major Braille producing country has different standards for cell spacing and dimensions. For instance, the United States Library of Congress adopts a Braille system that is standard throughout the USA (American National Standard, 1998), while the Department of Justice published revised regulations for Titles II and III of the American with Disability Act of 1990 in the Federal Register on September 15, 2012 (ADA, 2010).

Background and Perspective

Societies become increasingly interested in improving the welfare and well being of its disabled members. Concurrently, governmental regulations and many legislations are being set forth to promote a suitable environment where the blind or visually impaired

(BVI) individuals are easily integrated within their communities. This collective awareness in the official and local levels has triggered an unprecedented research effort that is directed towards the needs of the BVIs.

Neuroengineering and rehabilitation technologies are critical to ensure the BVIs can lead fulfilling and productive lives. The BVI need a portable and multifunctional device to conveniently assist them to hear and “see” (National Federation of the Blind, 2012). Although some audio devices and Braille displays are now available, e.g. the Kurzweil-National Federation of the Blind handheld Reader, these devices lack a fast, adaptive, and functionalized tactile rehabilitation display to enhance the abilities of the BVI to both read and perceive graphics. Without the featured tactile display, it is impossible for them to feel the diverse graphics/texture patterns or to sense essential tactile information such as temperature, roughness, and hardness. Moreover, the lack of portability of the currently available tactile display devices limits their ability to “see” and feel anytime and anywhere.

Statement of Problem

Existing Braille systems provide the BVI with technologies and tools to access and process information using devices such as: note takers, GPS systems, calculators, mobile phones, and print-reading devices. Most of the existing portable systems are heavy and/or costly. A technology resource list is provided by the National Federation of the Blind (National Federation of the Blind, 2012). Many of these Braille devices are portable (Braille Star 40 and 80, Braille Wave, Brailliant, BrailleConnect, Easy Braille, PAC Mate, and Seika); however these devices function as storage/playback devices. In addition, they use between 20 and 88 Braille displays, making them bigger in size, also they are relatively expensive ($2,000 – $14,000). The lateral force generated on the finger pad due to the physical contact with the Braille dots, and the sustained yet tedious pressure due to the repetitive Braille reading pattern may cause finger pad numbness and tingling. As a result, there is an increasing need to overcome these limitations to attain the sought welfare for the blind. It is suggested that a convenient, portable, wearable, light and small, yet budget-friendly device be developed.

The objective of this research is to design an affordable Braille tactile display that is wearable, refreshable, and portable. The device is intended to be used as an output device that can playback stored media. It can be also incorporated with current Braille reading technologies. The device will control both the electrical and mechanical stimulations to optimize the sensation and ensure extended use of the device. This work is concerned mainly with the mechanical aspects of the design. Other related issues of the electrical components design and control were presented (Fadali, Shen, & Jafarzadeh, 2009).

Literature Review

The objective of recent research effort on tactile sensation is to provide visually impaired persons with a more natural handling of their surrounding environment. Mechanical and electrical stimulations are responsible for generating the haptic perception. Numerous approaches exist to describe haptic perception through presenting some realization for the generated stimulations. Tactile sensation is usually divided into two major areas:

1. Haptic perception which involves identifying the surrounding bodies through touching of edges, curvatures, and texture. It also involves hand position and conformation.
2. Haptic-Braille which uses the haptic perception as a foundation for the recognition of the Braille characters.

Research conducted in this area can be divided into these tasks:

- Fingertip force measurements
- Haptic perception and braille reading
- Fingertip wearable haptic/braille devices
- Force sensing algorithm
- System control

The following is a brief overview of the recent research done in these areas.

Fingertip Force Measurements

Studying the force distribution on the fingertip helps in determining force resolution. Park, Kimt, and Shinichi, (2003) studied the force distribution on fingertip. They used a soft hemisphere-shape to model the fingertip. A compressional strain mechanism was developed for this case. This model was used to estimate the deformation and force distribution on the fingertip when loaded. Based on their results, they introduced a nonlinear model for the fingertip loading. Kamiyama, Kajimoto, Kawakami, and Tachi (2004) developed a tactile sensor that is capable of measuring the forces on the fingertip as well as the direction of these forces. The experimental approach was based on using of colored markers inside an elastic body and a color CCD camera. The movement of the markers, which was captured by the CCD camera, was used to identify the distribution of force vectors. The deformation of a soft fingertip is also investigated by Ho, Dao, Sugiyama, and Hirai (2008). First the deformation was simulated using ANSYS software using a non-linear finite element model. A realization of the experiment was achieved after this analysis. A 4-DOF micro Force/Torque (F/T) sensor was embedded inside the soft fingertip. Results measured by the F/T sensor matched the results of the model.

Blood volume beneath the fingernail has different patterns due to normal force, shear force, and finger extension/flexion, which is caused by the mechanical interaction between the fingernail and bone. This information was the motivation behind creating a fingernail sensor, (Mascaro & Asada, 2004), which can measure the two-dimensional pattern of blood volume beneath the fingernail. This technique was used to study the hemodynamic state of the fingertip when it is bent or pressed against a surface. A sensor with array of photodiodes distributed on it was created. The bending angle and touch forces were related to the optical sensor outputs through linear, polynomial, and neural network models. The authors designed a filter to predict the forces on the fingertip. Normal, lateral shear, and longitudinal shear forces as well as bending angle can be estimated through this technique. An alternative method was presented by Sun, Hollerbach, and Mascaro (2006), where an external camera was used. The surrounding skin around the fingernail is also included in this method. It was shown that the fingernail has a middle region with a low force range 0-2 N. The front region of the fingernail has an intermediate force range 2-6 N, while the surrounding skin has a range of 3-6 N or more.

Earlier research has shown that shear forces are responsible for the discrimination ability of the touch pads. Drewing, Fritschi, Zopf, Ernst, and Buss (2005) tested this ability for tactile movement through a four pin tactile array, which were able to move in the two tangential directions to produce enough shear force. Two experiments were conducted: single pin stimulation and multi-pin stimulation. Results showed that while test subjects were able to discriminate single pin movements, they were not able to discriminate each pin's movement independently in the multi-pin experiment. Normal forces are used to scan objects through parameters estimation and cost function optimization (Oh, Cho, Kang, & Kim, 2006). The index finger was fitted into a frame that is moving vertically. The speed at which the finger moves toward the object was varied, as well as the shape of the object to reach more generalized results. The normal force needed to scan the objects ranged between 0.75-0.9 N. Both normal and lateral forces are needed to receive proper stimulation on the fingertip's touch receptors. Usually these forces are not necessarily equal since touch receptors react differently to these forces. Kim, Choi, Kwon, and Kang (2006) developed a three-axial flexible tactile sensor that is used in a robot hand applications as grasping. The sensor was characterized using a 3-axis load cell by gradually applying a ramp force signal (0-0.6 N) and studying the sensitivity of the output load cell voltage. It was found that the magnitude of the sensitivity due to normal force is almost twice the sensitivity due to lateral force.

Watanabe, Oouchi, Yamaguchi, Shimojo, and Shimada (2006) measured the contact force during Braille reading. They addressed two challenging problems. First, the dependability of output values on the point of contact. Second, there is no universal method followed by users to read Braille. They used two transformation techniques to solve the first problem, and studied two manners of reading (one and two handed) to generalize their findings. It was found that the contact force ranged over time between 0.4N at the beginning, to 1.2N after 40 seconds of continuous reading. The experimental results showed that the contact force is a time dependent variable and that mechanical stimulation is limited by this fact.

Haptic Perception and Braille Reading

It is important to join both haptic perception and Braille reading for a flexible device. Haptic perception is considered the base for any subsequent Braille applications since the recognition and discrimination-ability generated in haptic are needed to recognize the dots arrangement and to identify Braille letters.

Ramstein (1996) combined haptic and Braille reading to recognize forms and texture using the sense of touch. A bi-dimensional single cell Braille display (Pantobraille) combining a force feedback device (FFD) with a standard Braille cell was designed. An interactive task was designed to follow reading patterns with one or two hands. A pantograph was used to move and read Braille by the subjects. The subjects were asked to read Braille while the cell was mounted on the pantograph using one hand for manipulation and reading. Then they were asked to use the same setup but using two hands. Finally the task was to put the cell aside and to manipulate using one hand and read using the other one.

Linear electromagnetic actuators that are used in refreshable Braille displays have been designed (Nobels, Allemeersch, & Hameyer, 2004). A Braille mouse was designed with the concept of a desk that has electromagnetically actuated pins through solenoids. The pins were arranged in a 3x2 arrays to form the Braille letter. While the desk moves, three letters are shown at a time through an opening in the housing while the rest of the pins are covered. Just before they entered the window, the pins were being set to disclose a predetermined letter. The user was to place his finger on the window and let the pins stimulate the fingertip. The pins were being reset after they leave the window.

Haase and Kaczmarek (2005) tested the perception of scatter plots using electrotactile presentation on the fingertip and the abdomen. The displays used consisted of electrodes covering the display area in a square matrix form. The experiment consisted of two parts, the first dealt with the ability to discriminate between different applied waveforms and their clarity level (rank) through the application of these waveforms on the fingertip and the abdomen. The waveforms (all pulse waves) differed in their base frequencies and pulse number. It was found that higher frequency and pulse number waves were highly ranked in both, fingertip and abdomen. The second test was the digit identification on both areas. The digit display size was larger for the abdomen, almost six times larger than the fingertip display. The same highly ranked waveforms were used and the results showed that the identification on the fingertip was better than on the abdomen.

Burton, McLaren, and Sinclair (2006) studied the activation of visual cortex in blind people through reading Braille. The subjects visual ability ranged between late blind (lost sight>5.5 yr), early blind (lost sight <5 yr), and sighted subjects. The idea was to study the visual cortex engagement of all groups and to study its similarity when reading by touch. The accuracy of identifying the letters were almost similar between groups, they differed slightly in the reaction times needed to identify letters, but the reaction times were similar for identifying words. Tactile sensation is a human factor that needs to be adjusted for different subjects. The study did not provide information about the technique used to insure proper contact force between finger and letters.

Force Sensing Resistors

The development of polymer film force sensing resistors (FSRs) has addressed the need to measure forces using relatively cheap and simple sensors. The electric resistance of an FSR is inversely proportional to the force applied at its surface. Recently, FSRs have been increasingly replacing classic force sensors in many areas including automotive industry such as, detecting presence and weigh of a passenger. They are also used in electronic devices such as joysticks and in scrolling and navigations. FSR can be also used for tactile application. In this work, FSR is a part of an electronic Braille reading device where it detects the force on the fingertip.

There exist many off-the-shelf FSRs of many shapes and sizes. However, design differences between these FSRs are mainly in the number, conduction medium, and arrangement of the layers, but they all share a common working principle. Only few works addressed these different sensors in terms of repeatability, time drift, hysteresis and robustness. Vecchi, Freschi, Micera, Sabatini, Dario and Saccchetti (2000) studied the Interlink's FSR (Standard 402) and the Teksan's FlexiForce (A201) sensors and proposed that the FlexiForce has better repeatability, linearity, and time drift, while the FSR is more robust. Lebosse, Bayle, Mathelin and Renaud (2008) also launched a comparison between FlexiForce (A201) and FSR (Standard 406) Interlink's sensor. They found that the FlexiForce exhibits more linear output than the FSR, and unlike the previous work by Vecchi et al (2000), they found the repeatability and the time drift of the FSR were better than the FlexiForce. Another evaluation study of three commercial FSRs was proposed (Hollinger and Wanderley, 2006). The work addressed the Interlink FSR (Standard 402), the FlexiForce (A201), and the LuSense PS^3 (Standard 151). It is found that the FlexiForce has the highest precision, the highest noise, and the slowest response. However, the FlexiForce's resistance drops from the nominal value for subsequent tests more than the other FSR's. They also recommended the FSR or PS^3 sensors if the application is composed of large varying forces at high frequencies.

Many works have discussed the problem of calibrating and modeling FSR's. In an attempt to study the biomechanics of the grasp and hand injury rehabilitation, Jensen, Radwin and Webster (1991) used FSR's that are directly attached to the subjects' fingertips. The subjects were asked to pinch a dynamometer for equally spaced force levels while the FSR's were calibrated. Regression analysis was then used to describe the force-voltage relation through a second order polynomial. A mathematical modeling of the FSR using cubic spline interpolation was proposed (Vaidanathan & Wood, 1991). In this work, they suggested that the overall polynomial approximation is highly affected by a local bad behavior of the system, and that cubic spline interpolation has the flexibility to describe such bad behaviors. An experimental study to model the FSR using regression analysis was addressed (Birglen & Gosselin, 1995). They used static loads of known masses to calibrate the FSR's resistance response into a reciprocal function. Zehr, Stein, Komiyama and Kenwell (1995) attempted at creating a linear region for the FSR to operate in through the implementation of an operational amplifier. They proposed that, through adding a proper resistance value in series with the FSR, the linear region can be expanded. However, the proposed method failed to describe the FSR's hysteresis. Florez and Velasquez (2010) discussed two FSR’s behaviors, creep and hysteresis. They suggested that a typical creep occurs at levels below 0.2 V/s, so they derived the voltage and compensated for any creep effect that is less than the threshold value. They have also suggested that the hysteresis is described by a fourth order voltage dependent polynomial. Another work (Hall, Desmoulin & Milner, 2008) aimed at calibrating and conditioning the FSR. First, they conditioned the FSR resistance through an operational amplifier to linearize it around a specific operating region. Then they assumed an output voltage, which is dependent on the loading history represented as a moving integral, to compensate for the hysteresis. Lebosse et al. (2008) modeled the nonlinear behavior of two commercial FSRs. They modeled the responses using regression analysis, while they modeled the FSR’s signal decrease over time as a function of its frequency, mean value, and amplitude.

Most of the literature in this field were dedicated either to model the static behavior of the FSR, or to assume regional linear response due to dynamic loadings. Neither of these approaches can be generalized, since loadings are dynamic in typical industry applications. In addition, the linear region of an FSR is bounded and cannot provide convincing description for the entire operational course. In today’s applications, these FSRs are implemented in different applications and they experience different working conditions. Thus, it is critical to mimic these working conditions in order to reach a general mathematical modeling that is less sensitive to the loading dynamicity.

Fingertip Wearable Haptic/Braille Devices

Incorporating Rehabilitation technologies for the BVI allows them to lead an independent and fulfilling life. Reading is one area where modern technologies are yet to be fully introduced. Currently, the BVI need a portable device to conveniently allow them to read. Although some portable audio devices are now available, e.g. the Kurzweil-National Federation of the Blind handheld Reader, these devices generally lack a fast and portable tactile rehabilitation display to enhance the abilities of the BVI to both read and perceive graphics. Without such tactile display, it is impossible for them to feel the diverse graphics/texture patterns or to sense essential tactile information. Moreover, the lack of the portability of currently available tactile display devices limits their ability to "see" and feel anytime and anywhere.

Different designs were developed for fingertip wearable haptic/Braille devices. A major objective of such devices is to ensure that appropriate contact force for mechanical stimulation is maintained. Contact force affects the amount of current flowing into the fingertip skin. As in most electrical stimuli, it is less accurate than mechanical stimuli (Bobich, Warren, Sweeney, Helms Tillery, & Santello, 2007), but at the same time it is spatial independent stimuli.

The following survey covers some of the recent design works in this area.

Minamizawa, Tojo, Kajimoto, Kawakami and Tachi (2006) built a wearable finger glove through the use of two motors and a belt. The target of the device is the pad of the middle phalanx through sensing and displaying haptic information. Sensitivity as well as the gravity issues were studied. To test the sensitivity, a setup of a board and two voice-coil type linear actuators that are responsible for driving the board horizontally and vertically is built. To examine the ability of displaying gravity sensation, the deformation of the middle phalanx of the finger was under investigation. To achieve this deformation, a motor with a pulley is connected to a belt that is in contact with the middle phalanx. The finger is placed in a mold to prevent its lateral and normal motions and to limit the motion of the belt in the lateral motion. There is sticky disk between finger and belt to prevent slipping and to ensure only deformation. The dorsal side of the finger is being fixed by the mold to allow the deformation of the finger through the motion of the belt and the sticky disk. Vertical stress and shearing stress are then reached through the use of a more general design. The design has two small motors setting on the top of the finger. They are attached to a board through belts. When the two motors have different rotational directions, a vertical stress is generated, while the shear stress is generated through same rotational direction of the motors. There are some problems associated with this design such as the insufficient pressure resolution. Some tactile is also felt at the dorsal side of the finger.

Koo, Jung, Koo, Nam, Lee and Choi (2006) dealt with the tactile display device based on soft actuator technology with ElectroActive Polymer (EAP). The material used has many advantages including flexibility, softness, and high power transmitted. It also can be modeled into many configurations due to its structural flexibility. This makes it easy to be designed so it can be worn at any part of the human body, including Braille devices for the visually disabled. They developed a tactile display device with 4x5 actuator array (20 actuator cells). The material exhibits compression in thickness and expansion in the lateral direction when a voltage potential is applied across the elastomeric polymer film coated with compliant electrodes on both sides. Mechanical actuation force is generated because of this contraction and due to the charged electrical energy across the thickness of the material. An incompressible elastomer block is attached between rigid boundaries. Voltage is applied across the elastomer, which causes the thickness in the axial direction to compress and thus the lateral in the radial direction to expand. This expansion in the radial direction causes concave bending of the elastomer film and enables mechanical stimulation. These types of actuators need high voltage to drive it (1to 2 *kV*), which makes it impractical to be used in the human interface applications.

Polyvinylidene Fluoride film (PVDF) is used as the sensory receptor (Tanaka, Miyata & Chonan, 2007). The sensor is mounted onto a fingertip and moved over Braille manually to obtain the sensor output. The sensor generates characteristic signals for each letter through the use of a piezoelectric PVDF film as the sensory material. Some of the characteristics of the PVDF film are that it has high sensitivity and is thin, lightweight, flexible and low cost. The setup consists of one sheet of PVDF film and is used as sensory receptor. The output is generated through the dynamic contact between the sensory receptor and Braille. The base of the sensor (stainless shell) houses –in parallel: a sponge rubber, a sheet of PVDF film with an electrode patch, and a protective plastic film. The sponge rubber is arranged such that its long side is perpendicular to the direction of motion of the sensor. Time of contact between the sensor and each dot in a vertical row varies based on the dot’s position, which makes signals of each class different in shape. Mechanical stoppers set on both upper and lower sides of the sensor surface to maintain constant contact depth. Guides are mounted at the side of the sensory receptor to prevent any vertical motion and to maintain straight motion along the Braille. Unsteady movements generate unsteady waveforms, which in turn need a robust recognition system. The mechanical stoppers limit the mechanical stimuli to a fixed depth, which may be less/more significant to some users.

CHAPTER 2

QUANTIFYING TACTILE FORCES IN THE HUMAN FINGER PAD

This study starts by presenting an approach to measure forces of the finger pad while reading Braille characters and to quantify the tactile acuity due to gender variations. The term ‘finger pad’ refers to that of the most distal pad on the index finger of the dominant hand. Fifty-seven healthy human subjects -- 28 males and 29 females -- participated. Each subject was asked to identify the dots arrangement for five individual Braille characters through touching the surface of each Braille character, and then sliding the finger pad over it. The experiment measures the reaction force between the finger pad and the dots in the touch mode. Reaction and the friction forces are measured in the sliding mode. The analysis presented in this study can be useful for the development of regulated tactile applications, such as Braille reading devices.

Material and Experimental Procedure

Subjects

The fifty-seven healthy subjects, 28 males and 29 females, volunteered to participate in this experiment. Their ages ranged from 18 to 35 years, with a median of 24 years. Only four of them (1 male and 3 females) were left-hand dominant. Majority of the subjects were students or young employees at the University of Nevada, Las Vegas (UNLV). The experimental procedures were approved by UNLV’s Office for the Protection of Research Subjects and the UNLV’s Institutional Review Boards (IRB). Each participant was asked to fill out a biographical information sheet and sign a consent form before the experiment was conducted. Biographical information that was collected included name, gender, age, and hand dominance.

All of the subjects were unfamiliar with the Braille characters. In order to calculate the finger pad pressures, the width and length of the finger pad were measured for each subject. The subjects were coded, and all forms were kept confidential under the possession of the Principal Investigator.

Tested Objects

A six-dot Braille system has each of the characters arranged in a rectangle containing two columns of three dots each. The pattern of each character consists of a unique combination of raised and lowered dots. Certain characters are designated into upper or lower dot patterns so that the raised dots appear only in the upper or the lower two thirds of the rectangle, respectively. Examples of these patterns are the alphabets ‘A’ through ‘J’, the numbers ‘0’ through ‘9’ and the punctuation signs.

In this study, the above patterns were excluded, and more standard forms of dots arrangements, in which the raised dots appear in the three rows, were selected. The five Braille characters selected for the experiment (M, N, O, P, and Z) have close arrangements of the dots as shown in Figure 1(a), which tests the ability of the subjects to discriminate between them. For example, all of these characters have raised dots in the first and third locations, three of them have a raised dot in the fourth location, and three have a raised dot in the fifth location. Since all subjects in this study were all healthy and sighted, the dots arrangement identification task was chosen to expose subjects to the same challenge and to ensure they will explore and identify the surface, rather than merely sliding their finger pads over it. Using a CNC machine, these characters were machined according to the specifications of the American Library of Congress (Braille Books and Pamphlets, 2005), as shown in Figure 1(b).

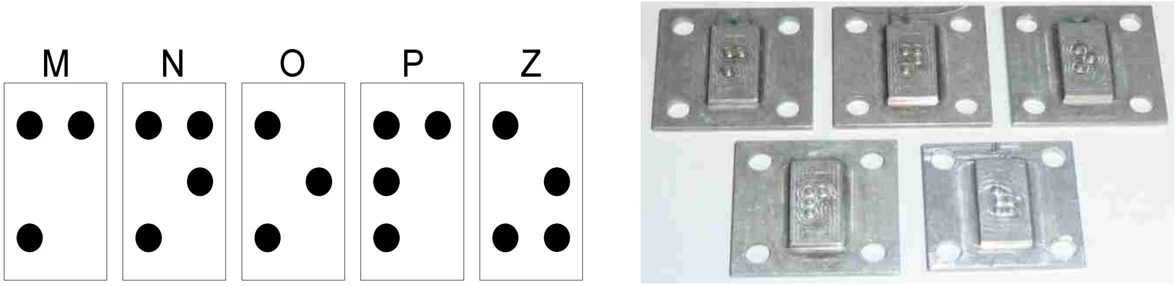

a. Images of Braille Characters b. Machined Braille Characters

Figure 1. Braille Characters Used in the Study.

Force Measurement

The main element of the experimental setup was the six-degrees-of-freedom force/torque sensor, an ATI Nano 17 (Nano 17, 2012). The sensor weighted 10 *gm*; it could be calibrated to measure a maximum force of 12 *N* in the XY plane and moments of 0.12 *N.m*, with 3.1e-3 *N* force and 1.6e-5 *N.m* moment resolutions. The force/torque sensor could provide a force/moment profile containing three forces and three moments in the Cartesian space, with a sampling frequency of up to 10 *kHz*.

The sensor was interfaced through an ATI data acquisition board, which was installed into a processing computer. The experimental data were analyzed using Fast Fourier Transform (FFT) analysis to determine the appropriate value of the filtering cut-off frequency. Figure 2 shows a typical FFT analysis of a force signal. Based on these results, it was determined that frequencies higher than 5 *Hz* could be filtered out.

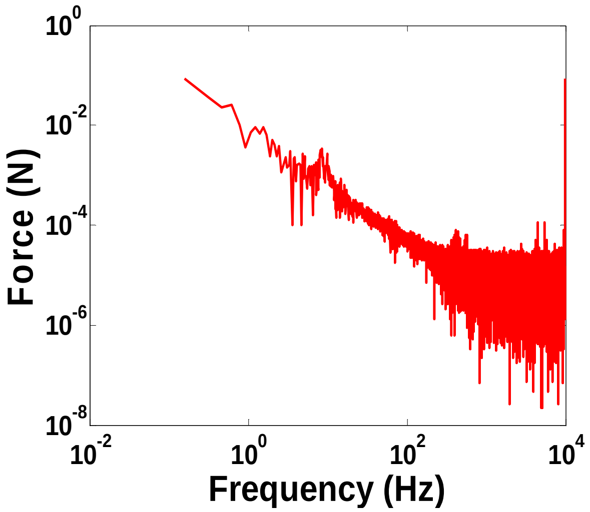

Figure 2. Fast Fourier Transform Analysis for Tactile Force.

Measuring System Configuration

The experimental setup was built to measure the contact force while reading Braille characters, as shown in Figure 3(a). The sensor was mounted on top of a base by using three mounting screws, and the sensor's base was attached to a rigid steel lab table by four screws. A metal Braille character base, attached to the top of the sensor, had four mounting columns to allow quick loading and unloading of the different Braille characters.

The sensor base had two slots on both sides of the sensor to allow the installation of two walls, as shown in Figure 3(b). The walls protected the sensor from any sudden force applied by the participants in this experiment. These walls were designed to keep the Braille characters hidden from view during the experiment, as shown in Figure 3(c).

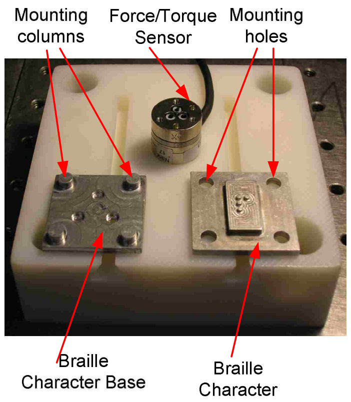

(a) Main Components of the Experimental Setup.

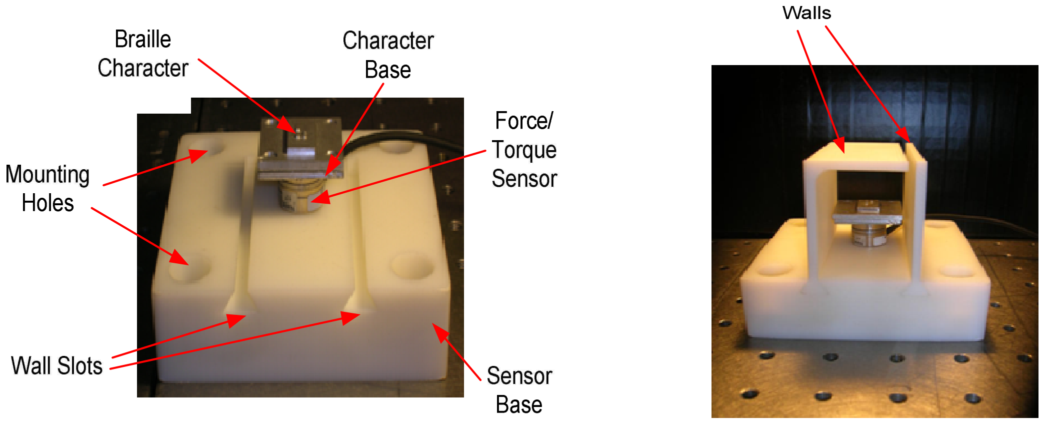

(b) Walls removed (c) Walls installed

Figure 3. Experimental Setup with Walls Removed and Walls Installed.

Braille Character Identification

As mentioned earlier, five Braille characters were used in each experiment. Immediately after each experiment was performed, each subject was asked to identify the touched Braille character out of a picture of the potential five Braille characters, shown in Figure 1(b). Each Braille character was presented once during testing. To ensure internal validity of this experiment, the following sequence of presenting the Braille plates was used: N, Z, M, O and P. The identification results are summarized in Table 1 and depicted in Figure 4. Although the subjects were Braille illiterate, the majority of them were able to identify some of the Braille dot arrangements by means of touch. The results show that females outperformed males in the character identification task, with a median of three successfully identified Braille dot arrangements compared to only two for the males.

Table 1. Identification of Braille Characters by Gender

		Number of Correct Identified Dots Arrangements						**Median**
		0	**1**	**2**	**3**	**4**	**5**	
Subject Frequency	**Male**	4	5	7	3	4	5	2
	Female	3	4	5	11	5	1	3

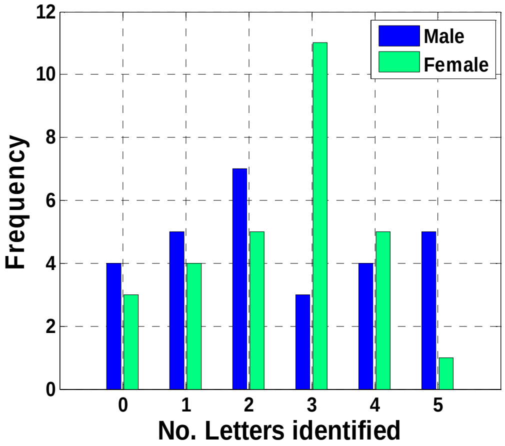

Figure 4. Results of Braille Character Identification

Methodology

After having a participant fill out the biographical information sheet and consent form, the investigator asked the participant to sit at a testing table, clearly explained the tasks to him or her, and answered any questions the subjects may have had. Each subject was given a practice test (1-2 min) to familiarize the finger pad with the five Braille characters, and to prevent during actual testing disturbed motion of the finger pad due to the lack of information about the surface. Throughout the entire experiment, each subject was seated on a desk chair that faced the experimental table, with the hip and knee joints flexed at 90^{o} degrees and the back straight. The arm was adducted and flexed forward at the shoulder joint, and the elbow was extended with the forearm pronated and resting on the experimental table.

Each subject placed the finger pad above a Braille character that was hidden from the subject’s view, but without contact, as shown in Figure 5(a). The force recording started when the investigator signaled to the subject by a voice command to start the touching mode; at that point, the subject lowered the finger pad and maintained proper contact force with the Braille dots, as illustrated in Figure 5(b). The six components of the force/moment tensor time history in Cartesian space, as shown in Figure 5(c), were recorded for about 10 seconds.

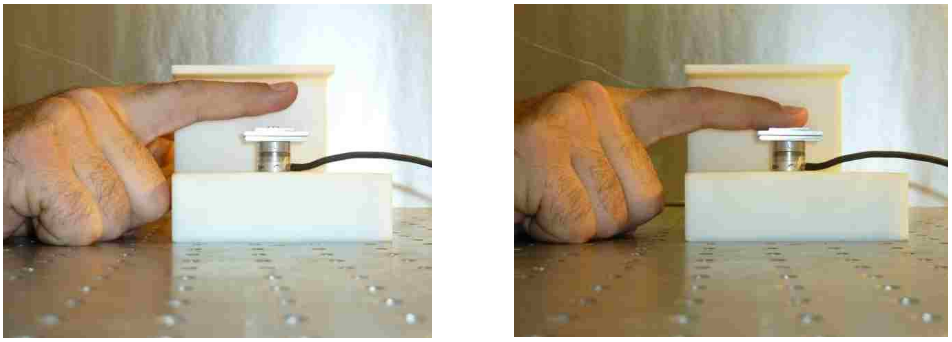

(a) Position of the finger pad before the touching mode.

(b) Position of the finger pad during the touching mode.

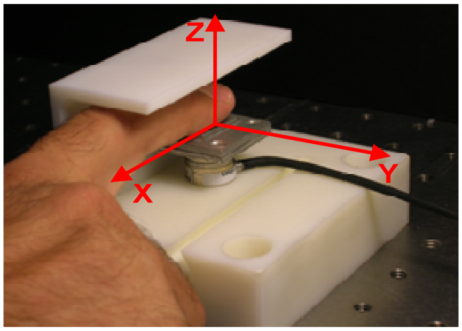

(c) Configuration of the Cartesian space.

Figure 5. Finger Pad Positioning; One Wall is Uninstalled for Visibility of the Setup.

The subject was then asked by a second voice command to remove the finger pad, while the investigator stopped recording forces and prepared the experiment for the next task. The subject was asked by a third voice command to start the sliding mode by sliding the finger pad along the surface of the Braille character from left to right. Another set of the six components of the force/moment tensor time history were recorded. At the end of this process, the subject signaled to the investigator that the sliding mode had ended. At this point, the investigator stopped recording force, which typically lasted between 5 and 10 seconds. After that, the subject was introduced to several images of Braille characters, as shown in Figure 1(a), and was asked to identify the dot arrangement of the character he or she had touched. These steps were repeated for each of the remaining characters. Figures 6 and 7 show the forces and moments time histories in the touching and sliding modes, respectively, for Subject 1 while testing the Braille character ‘N’.

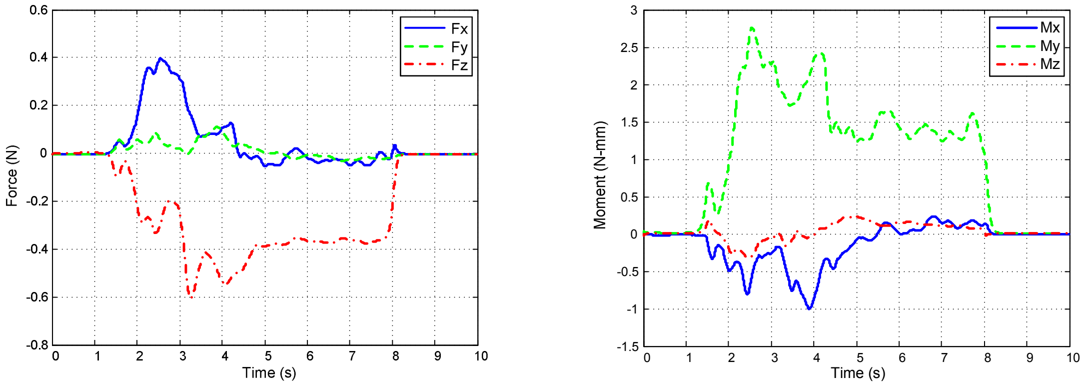

a) Force profiles b) Moment profiles

Figure 6. Force and Moment Profiles for Subject 1 While Identifying Braille Letter ‘N’ in Touching Mode.

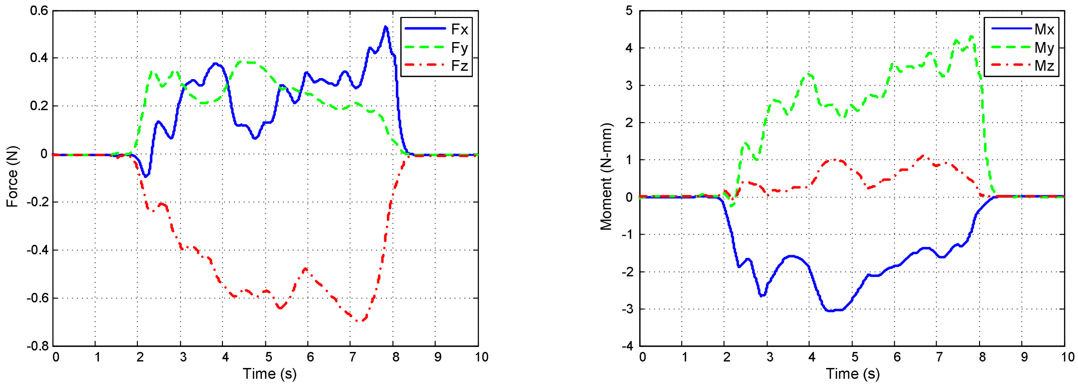

a) Force profiles b) Moment profiles

Figure 7. Force and Moment Profiles for Subject 1 While Identifying Braille Character ‘N’ in Sliding Mode.

Criteria for Characterizing Finger Pad Force Ranges

The selection procedure was divided into two categories for detecting touching and sliding modes of the finger pad separately. If the procedures failed to define a stable region in a force profile, that force profile was ignored and dropped from calculations.

Finger Pad Touching Mode Criteria

When the touching mode starts, the finger pad moves downward to create a physical contact with the surface. The finger pad undergoes mechanical deformation; as a result, a reaction force between the finger pad and the surface of contact is generated in the normal direction (F_{Tz}). The subject adjusts the level of deformation to achieve better comfort and recognition of the contact surface.

This study proposes that a steady F_{Tz} is associated with a minimal variation of the moment around the Z-axis, M_{Tz}, in other words, minimal twisting of the finger pad. This condition is achieved by monitoring the time derivatives of F_{Tz} and M_{Tz}. Based on studying the force and moment time histories for the subjects, a force interval was selected that corresponds to:

$$\left|\frac{dF_{Tz_{i,j}}(t)}{dt}\right| \leq 0.25 \quad \frac{N}{s} \qquad t \in \left(t_0, t_f\right) \qquad (2.1)$$

$$\left|\frac{dM_{Tz_{i,j}}(t)}{dt}\right| \leq 0.5 \quad \frac{N.mm}{s} \qquad t \in \left(t_0, t_f\right) \qquad (2.2)$$

where *i* is the subject's number and *j* is the Braille character's number.

A typical Braille reader, using either one hand or two hands, can read 60-120 words per minute (Mousty & Bertelson, 1985), which corresponds to 0.1-0.2 sec per letter. Since the subjects in this experiment had no prior experience with the Braille reading, a stable force interval of at least 0.15 seconds satisfied the criteria, ensuring the validity and consistency of the force readings.

$$\left(t_f - t_0\right) \geq 0.15\, sec \qquad (2.3)$$

Figure 8 shows the result of differentiating F_{Tz} and M_{Tz} signals of Figure 6 with respect to time. The identification period, based on the above criteria, also is marked. Comparing Figures 6 and 8 indicates that at 2.73 seconds, Subject 1 applied regulated force to touch the surface of the Braille character. In this case, the duration of the force identification phase was 0.199 seconds.

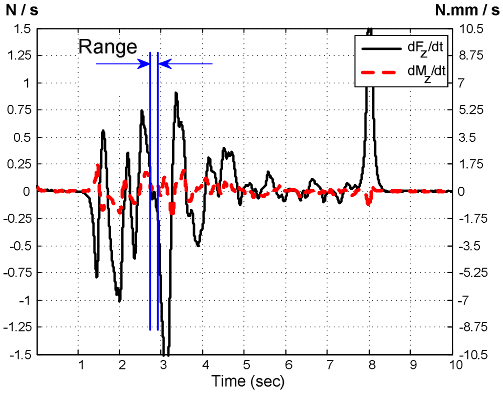

Figure 8. Differentiation of the Touching Mode F_{tz} and M_{tz} (From Figure 6) with Respect to Time.

Finger Pad Sliding Mode Criteria

Typically, the sliding forces are responsible for the detection of the dot arrangement and thus for identifying a Braille character (Miyata, Tanaka, Nishizawa, & Chonan, 2006). Unlike the touching mode, which is static, the sliding mode involves dragging the subject's finger pad on the dots to stimulate tactile receptors. Two primary forces are involved in identifying the dot arrangements of a Braille character: the tangential, or drag, forces (friction) and the normal forces (reaction). These forces are labeled, F_{Sy} and F_{Sz}, respectively, as shown in Figure 10.

Earlier studies have shown that unskilled readers are more likely to apply fluctuating finger pad forces while identifying Braille characters (Watanabe et al., 2006). Thus, the proposed criteria for this study compensated for this relatively high variation by relaxing the force and moment conditions. Studying the subjects' data through the sliding mode indicated that the steady F_{Sy} and F_{Sz} forces are associated with a limited variation of the moment around the Y-axis, M_{Sy}. This may indicate a minimal pressure of the finger pad. This phase is determined by monitoring the time derivatives of F_{Sy}, F_{Sz}, and M_{Sy}. Based on studying the force and moment time histories for the subjects, a valid force interval was selected that corresponded to:

$$\left|\frac{dF_{Sy_{i,j}}(t)}{dt}\right| \leq 0.5 \quad \frac{N}{s} \qquad t \in (t_0, t_f) \tag{2.4}$$

$$\left|\frac{dF_{Sz_{i,j}}(t)}{dt}\right| \leq 0.5 \quad \frac{N}{s} \qquad t \in (t_0, t_f) \tag{2.5}$$

$$\left|\frac{dM_{Sy_{i,j}}(t)}{dt}\right| \leq 1.0 \quad \frac{N.mm}{s} \quad t \in (t_0, t_f). \tag{2.6}$$

Similar to the previous section, the force duration is governed by the inequality:

$$(t_f - t_0) \geq 0.15 \text{ sec} \tag{2.7}$$

Figure 9 shows the result of differentiating the time histories of F_{Sy} and of M_{Sy} (Figure 7) with respect to time for Subject 1, while testing Braille character 'N'. The range selected is marked as well. Using the above criteria, this subject identified the Braille character at 4.38 seconds, as can be inferred by comparing Figures 7 and 9. The duration of the force identification phase for this subject was 0.274 seconds. The initial time and duration of the force identification varied among different subjects for the same Braille character, and also varied between different Braille characters for the same subject.

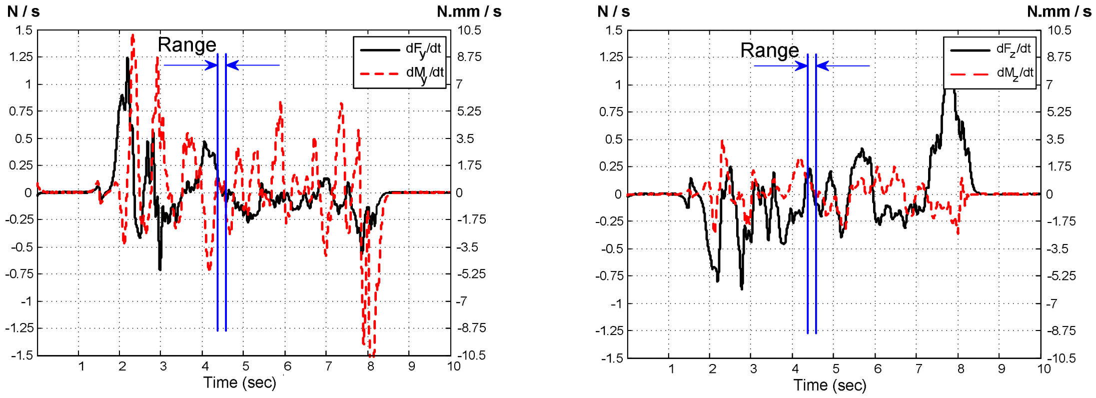

a) Differentiation of F_{Sy} and M_{Sy} b) Differentiation of F_{Sz} and M_{Sz}

Figure 9. Differentiation of the Sliding Mode Forces and Moments (From Figure 7) with Respect to Time.

Procedure for Aggregating Results from Individual Subjects

The valid forces collected from each subject, according to the aforementioned criteria, were detected at different time periods. Thus, the forces that resulted from each subject were clustered together for the sake of easy comparison. For instance, Figure 10(a-c) show the different touching and sliding forces for Subject 1, plotted using their absolute time scales (i.e., $t_f - t_0$). This approach eases comparison of the force time histories by ensuring that all forces have a common starting point at the origin.

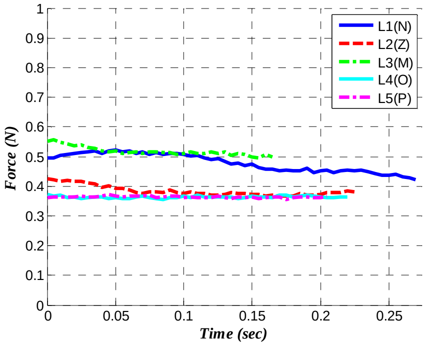

a) Touching Forces Z (F_{Tz})

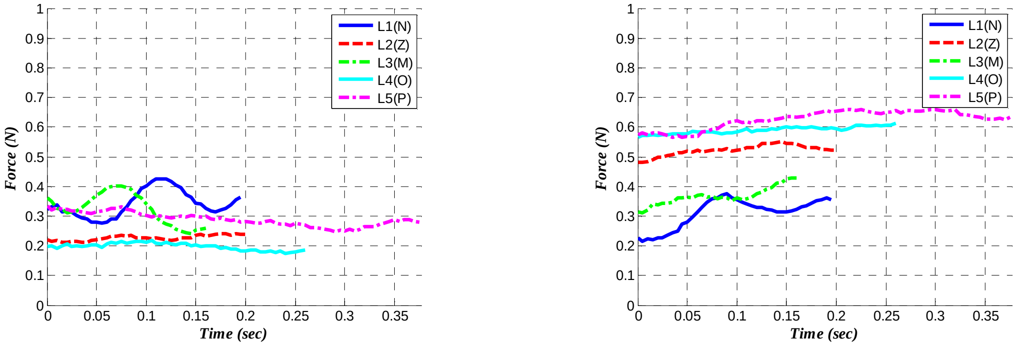

b) Sliding Forces Y (F_{Sy}) c) Sliding Forces Z (F_{Sz})

Figure 10. Force Time Histories for Subject 1.

The forces were linearized to facilitate further assessment. The means of these linearized force curves were computed for each subject, as follows:

$$F_{Tz_i} = \frac{\sum_{j=1}^{n} F_{Tz_{i,j}}}{n} \tag{2.8}$$

$$F_{Sy_i} = \frac{\sum_{j=1}^{m} F_{Sy_{i,j}}}{m} \tag{2.9}$$

$$F_{Sz_i} = \frac{\sum_{i=1}^{m} F_{Sz_{i,j}}}{m} \tag{2.10}$$

where *n* and *m* are the maximum number of forces passing the aforementioned criteria for subject *i*, and F_{Tz_i} is the average *Z* force component in the touching mode experiment for subject *i*. Similarly, F_{Sy_i} and F_{Sz_i} are the average *Y* and *Z* force components, respectively, in the sliding force experiment for subject *i*.

The finger pad pressures were calculated as follows to understand if forces and pressures are consistent:

$$P_{Tz_i} = \frac{F_{Tz_i}}{A_i} \tag{2.11}$$

$$P_{Sy_i} = \frac{F_{Sy_i}}{A_i} \tag{2.12}$$

$$P_{Sz_i} = \frac{F_{Sz_i}}{A_i} \tag{2.13}$$

where A_i is the area of the finger pad of subject *i*.

The means of the forces and pressures for the subjects in the touching and sliding experiments were grouped according to gender in order to study the influence of gender on human tactile forces.

Numerical Analysis

All statistical analyses for this study were carried out using the MATLAB® 2010a Statistics Toolbox (MathWorks, Natick, MA). Throughout this study, the level of significance was set at ($p < .05$). As outlined in Equations 2.1-2.7, the success rates for touching and sliding mode forces that exceeded the criteria are shown in Table 2.

Table 2. Percentage of Valid Tactile Forces

Gender	Sliding Forces	Touching Forces
Male	%75.71	%89.29
Female	%81.38	%95.86

The higher failure rate of the criteria in the sliding force experiment was due to the dynamic behavior of forces in the sliding mode, which creates more variation about the nominal values. To study the dynamics of all the tactile forces, a paired difference t-test was conducted to compare the slopes of F_{Tz}, F_{Sz}, and F_{Sy} for same subjects. Results showed that the slope of F_{Tz} was significantly lower than the slope of either F_{Sz} ($p = .002$) or F_{Sy} ($p = .001$) for females and F_{Sz} ($p = .007$) or F_{Sy} ($p < .001$) for males. The dynamic nature for some of these sliding forces may deny the stability condition set by the criteria as outlined in Equations 3-5. Table 2 also indicated that in general, female tactile forces have slightly better success rates than for males.

A one-sample Kolmogorov-Smirnov (*K-S*) test was used to compare data to a standard normal distribution. Results indicated that there was insufficient evidence to reject the normality hypothesis of the experiment's data, as shown in Table 3.

Table 3. Results of Normality Test

Gender	**Population Proportion, p_{value}**		
	F_{Tz}	**F_{Sz}**	**F_{Sy}**
Male	.857	.739	.806
Female	.259	.353	.883

This work proposed a numerical approach to test the following conjectures:

I. Male subjects have higher thresholds for tactile forces than female subjects.

II. After normalizing these forces, the pressure thresholds of male subjects remain higher than those for female subjects.

In testing Conjecture I, Table 4 shows a comparison between male and female tactile forces. To test Conjecture II, the data from Table 4 were normalized, as presented in Table

5. Finger pad surface areas for both genders were compared, as shown in Table 6. A two-sample t-test was used to check if the means for any two independent data sets were equal, as shown in Tables 4 through 6.

Table 4. Results of Tactile Forces

		Gender	**Level of Conf.**	**Mean (*STD*) (N)**	**Confidence Interval (N)**	**Right tailed t-test *p*-value**
Touching Mode	**Normal Force, F_{Tz} (N)**	Male	95%	0.786 (*0.448*)	0.613-0.959	***p* = .305**
		Female	95%	0.721 (*0.512*)	0.523-0.918	
Sliding Mode	**Normal Force, F_{Sz} (N)**	Male	95%	0.431 (*0.233*)	0.341-0.521	***p* = .011***
		Female	95%	0.300 (*0.182*)	0.230-0.370	
	Tangential Force, F_{Sy} (N)	Male	95%	0.418 (*0.200*)	0.340-0.495	***p* = .189**
		Female	95%	0.376 (*0.153*)	0.317-0.435	

*significant difference

Table 5. Results of Tactile Pressures

		Gender	**Level of Conf.**	**Mean (*STD*) (N/m^2)**	**Confidence Interval (N/m^2)**	**Right tailed t-test *p*-value**
Touching Mode	**Normal Pressure, P_{Tz} (N/mm^2)**	Male	95%	1834 (*898*)	1487-2180	***p* = .824**
		Female	95%	2182 (*1770*)	1500-2866	
Sliding Mode	**Normal Pressure, P_{Sz} (N/mm^2)**	Male	95%	1001 (*492*)	811-1191	***p* = .200**
		Female	95%	884 (*550*)	672-1097	
	Tangential Pressure, P_{Sy} (N/mm^2)	Male	95%	988 (*452*)	813-1163	***p* = .843**
		Female	95%	1119 (*522*)	918-1321	

*significant difference

Table 6. Results of Finger Pad Surface Area

	Finger pad area mm^2		**Right tailed t-test *p*-value**
	Mean	***STD***	
Male	423	*70*	**$p < .001$***
Female	348	*64*	

*significant difference

As pointed out earlier, the feeling of touch at a finger pad mainly is due to the reaction force F_{Tz} between the finger pad and the surface of contact. This force dominates the two other components in the touching mode experiment. On the other hand, the discrimination of surfaces is induced by two main forces (F_{Sz} and F_{Sy}), which generate from the sliding motion of the finger. The results of Table 4 for both male and female subjects indicate that for the same gender group, the magnitude of the normal force in the touching mode (F_{Tz}) is higher than the two sliding mode forces (F_{Sz} and F_{Sy}). The results of one-way ANOVA test indicate that the difference between F_{Tz} and the double of either F_{Sz} or F_{Sy} is not significant for male (p = .808) and female (p = .322) subjects. Figures 11(a-b) show the box plots for all these tactile forces.

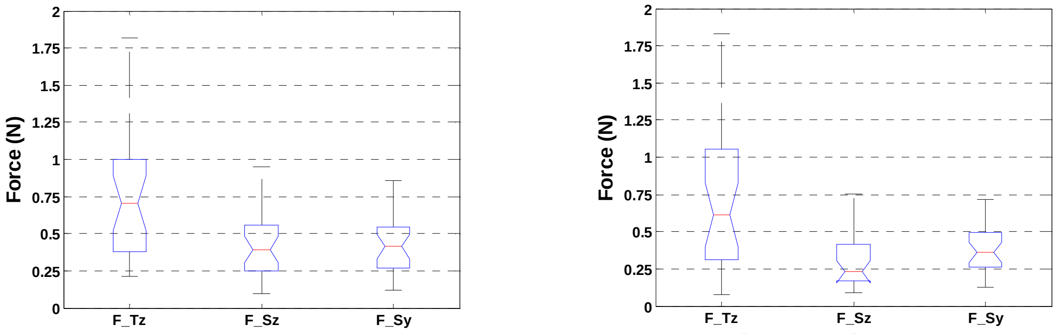

(a) Male Forces (b) Female Forces

Figure 11. Boxplot for Male and Female Tactile Forces (F_{Tz}, F_{Sz} and F_{Sy}).

Results of Table 4 indicate that only one force in the sliding mode, F_{Sz}, is significantly higher for males than for females. Although the other two forces, F_{Tz} and F_{Sy}, are slightly higher for males than for females, these differences are not statistically significant. While they are not significant overall, these differences still indicate that females experience higher conformability to surface geometry, as suggested earlier (Nakatani, Kawasoe, & Denda, 2011).

In order to test Conjecture II, the forces shown in Table 4 were normalized, and the equivalent tactile pressures were calculated. The differences between the three pressures (P_{Tz}, P_{Sz} and P_{Sy}) for male and female subjects were not significant, as shown in Table 5. Thus, there was insufficient evidence to support Conjecture II. That is, gender was not a deterministic factor in tactile pressure thresholds. In fact, comparing results from Tables 4 and 5 showed that the differences found in F_{Sz} in the sliding mode experiment was due to the smaller finger pad surface area of females but not due to gender. This became evident when the forces were normalized to eliminate the effect of finger pad's size: the difference between the two pressures (P_{Tz}) diminished. Although they were not significant, two of the pressures (P_{Tz} and P_{Sy}) for females were slightly higher than those for males. The previous findings suggest that females enjoy greater tactile acuity than males due to their smaller finger pad surface area, which may result from the dense concentration of mechanoreceptors but not due to gender.

As in the force analysis, pressure variances between males and females were addressed. Results of Table 6 showed a significant difference in the finger pad surface area between male and female subjects. However, these variances seemed to be homogenous.

CHAPTER 3

SENSING ELEMENT: FSR TECHNOLOGY

Introduction

A Force Sensing Resistor (FSR) is a conductive polymer that exhibits a decrease in resistance as the force applied at its surface increases. Several FSR commercial designs exist, where the main differences between these designs are in the structure of the layers and the active sensing material used.

Significance of Analysis

Most of the literature in this field were dedicated either to model the static behavior of the FSR, or to assume regional linear response due to dynamic loadings. Neither of these approaches can be generalized, since loadings are dynamic in typical industry applications. In addition, the linear region of an FSR is bounded and cannot provide a convincing description for the entire operational course. In this work, several linear and nonlinear models using two different approaches were proposed. System identification techniques are used to propose other forms of linear and nonlinear models of the FSR.

Of particular interest to this study is to identify the FSR for implementation in a refreshable and wearable E-Braille reading device. The device is composed of a refreshable 3x2 tactile array that is printed on an electrotactile display, which is actuated by a miniature DC motor that lifts and lowers the electronic board. This linear motion brings the display into contact with the index finger’s pulp to start the electronic transmission of data through the electrotactile display. FSR is installed beneath the electrotactile display to measure the contact force felt at the user’s finger. The measured force will be used in a feedback control loop to maintain a steady contact pressure between the finger pad and the display throughout the reading process. The range of the tactile forces while identifying five different Braille characters was identified experimentally in the previous chapter. Thus, the range of the forces measured were used to identify the FSR.

The Interlink's FSR is composed of two membranes. One membrane has two sets of electrically-distinct interdigitating electrodes. The other membrane holds the printed carbon based ink of the FSR. A spacer adhesive is applied between the two membranes to hold them together and to ensure the air gap between them is maintained. A spacer material, like a double-sided stick adhesive, is placed between the two films. Figure 12(a) shows how the layers of a typical FSR are arranged.

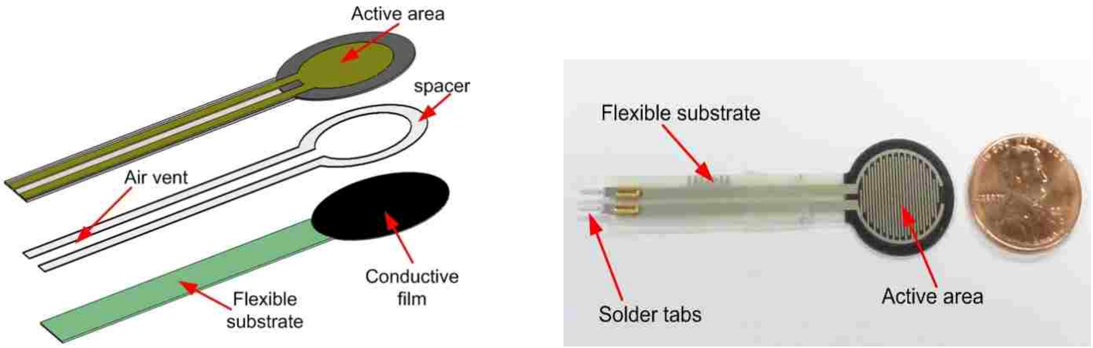

a) Layers Arrangement b) Physical Size and Geometry

Figure 12. FSR 402

In this work, an experimental approach to identify Interink's FSR Standard 402 (Interlink Electronics, 2012) was proposed. The selected FSR is a miniature rounded sensor that has solder tabs for easy connection, as shown in Figure 12(b). Table 7 shows the characteristics of the selected FSR. The dimensions of the FSR 402 are outlined in Table 8.

Table 7. Characteristics of FSR 402 (Interlink Electronics, 2011)

Feature	**Value**
Wide Force Sensitivity Range	0.1-10 *N*
Active Area (diameter)	12.70 *mm*
Thickness range	0.2 – 1.25 *mm*
Stand-off Resistance	> 10$M\Omega$
Hysteresis	+10%
Temperature Operating Range	-30 - +70 ^oC
Number of Actuations (Life time)	10 Million tests

Table 8. Dimensions of the FSR 402 Circular Part

Parameter	**Value**
Overall Diameter (D_c)	18.24 *mm*
Diameter of actuated area (D_{ac})	10.80 *mm*
Thickness (t)	0.5334 *mm*

An FSR works as an open circuit at no load, and when pressure is applied at its active surface the flexible substrate deforms. This allows the top substrate to be pushed against the bottom substrate, which causes the resistance to drop. If characterized properly, this drop in resistance can be utilized to measure the force applied at the FSR’s surface. FSRs are passive resistors that are usually configured in voltage divider circuits for simple resistance-to-voltage conversion, as shown in Figure 13.

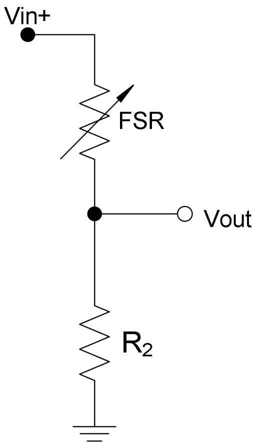

Figure 13. FSR'S Voltage Divider Circuit

A pressure that is applied at the FSR's surface will cause a drop in its resistance, which causes an increase in the voltage read between the circuit's terminals, as given below.

$$\boldsymbol{V_o = V_{in}\left(\frac{R_2}{R_2+R_{FSR}}\right)} \qquad (3.3)$$

Depending on the application requirements, an operational amplifier can be installed at the output's terminal of the voltage divider. Figure 14 shows how the FSR's resistance drops with the application of force at its surface.

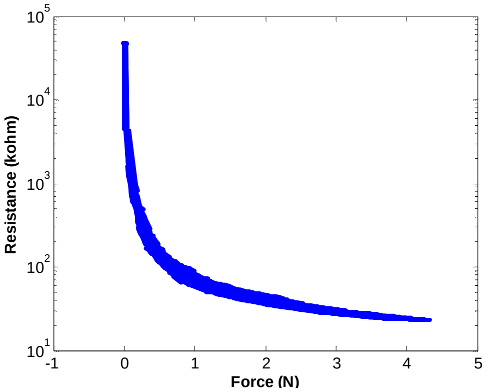

Figure 14. A Typical FSR'S Response due to External Force

Experimental Setup

An experimental procedure where the FSR is exposed to different displacement profiles is designed to identify possible models of the FSR. A component characterization device (Bose TestBench Instruments, 2012), Figure 15, is used throughout this work. This device has a high resolution actuator (minimum controllable displacement $1.5*10^{-3}$ *mm*) and is equipped with a low range (5 *lbs* ≈ 22*N*) miniature load cell (Honeywell, 2012). The linear actuator is used to generate different displacement profiles to mimic various tactile forces.

Figure 15. Component Characterization Device

A fixture is designed to ensure proper reading of the FSR, Figure 16(a). The FSR is placed on one part of the fixture, which has a solid flat surface to ensure an even force distribution on the FSR's active area. Double-sided adhesive is used to hold the FSR to the fixture. The second part of the fixture is attached to the end of the actuator, where a prototyped cylindrical actuator was attached to the motor side to position the pressure onto the FSR's active area.. The FSR's terminals are connected to a voltage divider (Voltage Divider, 2012), as shown in Figure 16(b). One of the external channels of the device is used to read the voltage divider circuitry. The voltage divider has an adjustable resistance (1-20) $k\Omega$ which can control the sensitivity of the output. A potentiometer that is integrated within the voltage divider is used to tune the resistance R_2 of Figure 13. The voltage divider is then connected to the PCI conditioning module via VGA male connector (15-pin HD D-Sub).

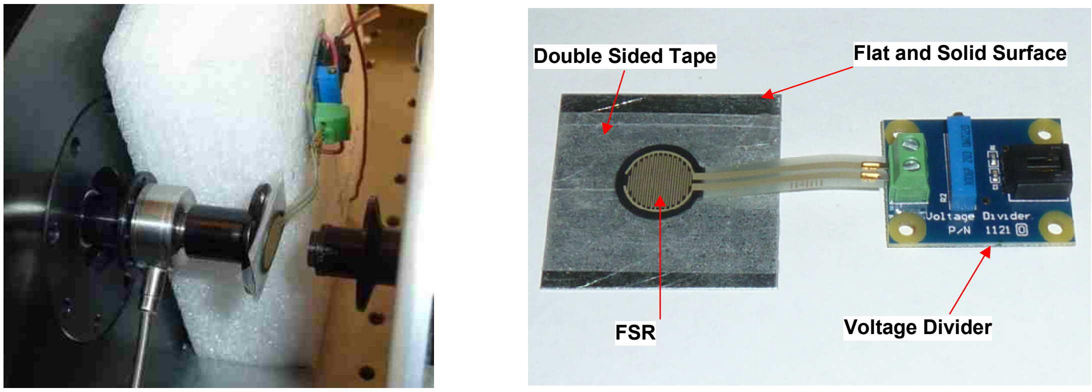

a) Experimental Fixture

b) FSR Interfaced with the Voltage Divider

Figure 16 FSR Testing Fixture

The reaction bracket of the testing system was used to fix the load cell and the FSR to the testing table. This reaction bracket is designed to allow the specimen to be attached in the horizontal or vertical configuration, and it is equipped with a micro-adjuster for easier specimen positioning. Figure 17 shows the experimental setup. At each experiment, the applied displacements, the resulting forces, and the corresponding FSR voltages are measured.

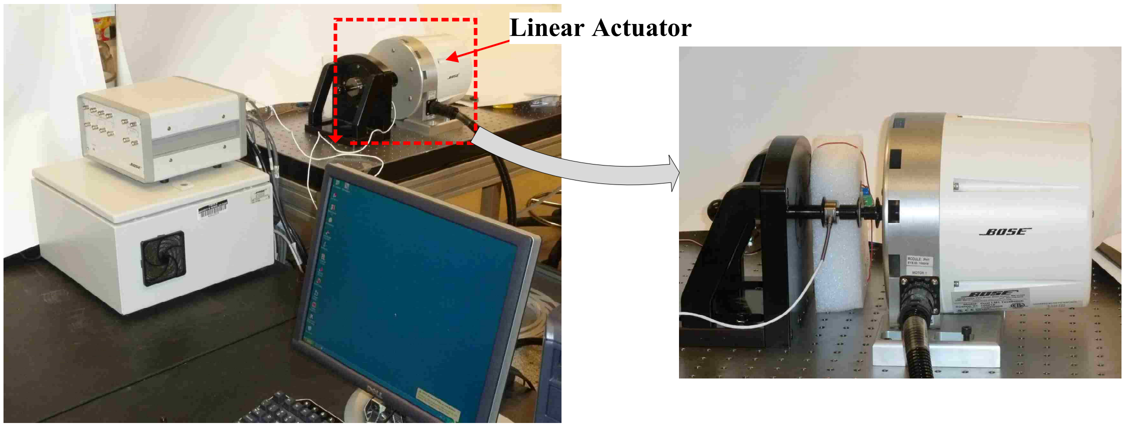

Figure 17. FSR Experimental Setup

Experimental Data and Signal Conditioning

Tactile forces are the forces induced by a human's finger pad to recognize haptic and read Braille. In the previous section of this study (Chapter 2), a system was developed to measure these forces. It was found that the tactile force amplitude varies among subjects, but in general it ranges between (0.2-2.0*N*) with some outliers that reach the 3.0*N* mark. The displacement profiles in this work are selected to represent this force range. The identification process starts by applying static displacement at the FSR's surface for an extended period (≈ 30 minutes). These loads are used to calibrate the FSR and study its time drift. Results depicted in Figure18 show that the FSR's response is fairly steady. The resistance however exhibits a small time drift (creep) in the order of +6%, which confirms the results of (Florez & Velasquez, 2010).

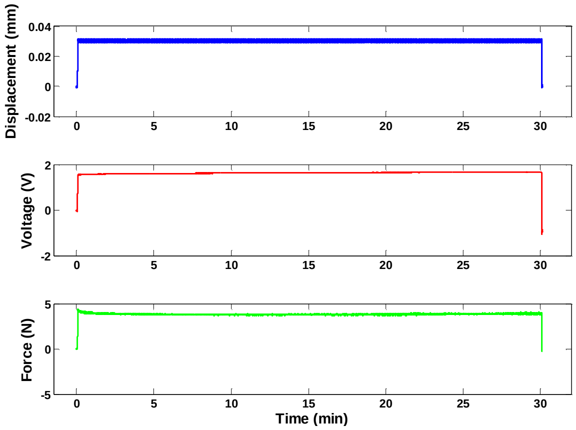

Figure 18. Results of the Static Loading Experiment

During the transition from no-load to load states, the FSR's resistance drops significantly as illustrated in Figure 14. Proper consideration should be taken to exclude this transition as it may deprive the current analysis. Thus, all data are recorded while the actuator's effector is always in physical contact with the FSR's active surface (even with the absence of external loadings). Physical equilibrium offsets appear in the data since the FSR is always under compression. Therefore, all recorded profiles are de-trended by removing the physical equilibrium offsets that appear before external displacements are applied. This is an essential step to estimate more accurate models (Ljung, 2011).

After calibrating the experiment, the identification process continues with the second phase to identify the dynamics of the FSR. On average, a Braille reader can read 60-120 words per minute (Mousty and Bertelson, 1985), which corresponds to 0.1-0.2 *sec* to identify a Braille character. Hence, an up chirp sinusoidal signal (0.2 - 20 *Hz*) is applied at the FSR's surface to investigate the dynamics of the system. The chirp signal starts at 0.2 *Hz* frequency with 0.1 *Hz* increments till 1.0 *Hz*, then with a 1.0 *Hz* increment till 20 *Hz*, as shown in Figure 19.

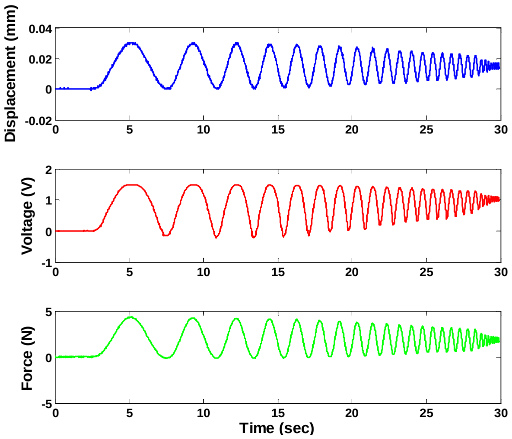

Figure 19. Dynamic Loading Experiment

All loadings are sampled at frequency of 100 *Hz*. A Fast Fourier Transform (FFT) analysis was conducted for the FSR's voltage to determine the filtering cut-off frequency, as illustrated in Figure 20.

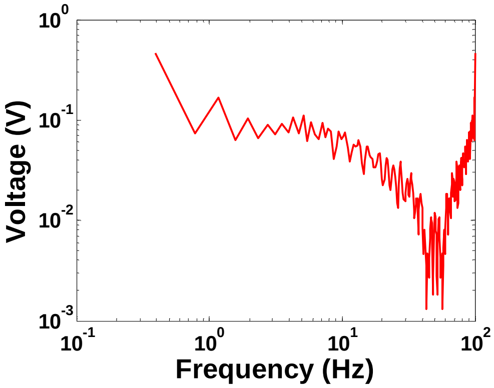

Figure 20. FFT Analysis for the FSR Voltage

Based on these results, it is determined that frequencies higher than 40 *Hz* should be filtered out. In addition to the chirp signal, other displacement profiles typical of tactile applications are used to assess the identification process. These profiles are: Square (0.1 and 0.2 *Hz*), Triangle (0.1 and 0.25 *Hz*), and Step (0.1 *Hz*).

Dynamic Mechanical Analysis (DMA) Test

In the DMA test, the FSR is subjected to cyclic excitations at different frequencies to study its mechanical characteristics. The DMA is used to determine the parameters of the second-order system model of the FSR, stiffness (k) and damping (c), Figure 21. The test monitors the displacement input and the force output and calculates the values of k and c that best fits the input and output data.

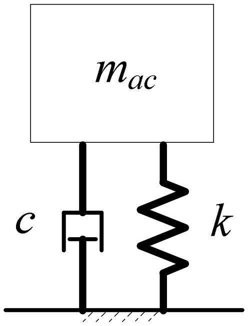

Figure 21. FSR Mathematical Modeling

The mass m_{ac} refers only to the segment of the FSR that is actuated by the DMA test, as shown in Figure 22. To calculate this mass, the FSR terminals were trimmed and the mass of only the circular part (m_c) was measured. It was assumed that this part is homogenous, thus the mass of the actuated material, which has a diameter (D_{ac}) can be given as,

$$m_{ac} = m_c \left(\frac{D_{ac}}{D_c}\right)^2 \tag{3.2}$$

where D_c is the overall diameter of the FSR's circular part.

Based on the above analysis, the mass of circular area (m_c) is 0.1401 *gm* and the mass of actuated area (m_{ac}) is 0.0491 *gm*. To ensure the validity of the results, the DMA test was repeated for the same FSR (24 hours later) and the results are presented in Table 9.

The results of Table 9 showed that both tests generated fairly close results (the maximum difference is less than 6.5%). The data were averaged and fitted using regression analysis, and the following formulas were generated:

$$c = 53.96\,f^2 - 44.44\,f + 10.81 \tag{3.3}$$

$$k = 23.82\,f + 94.32 \tag{3.4}$$

where f is the frequency of the actuation forces.

Figures 23.a and 23.b show the experimental and fitted data for the damping and stiffness, respectively.

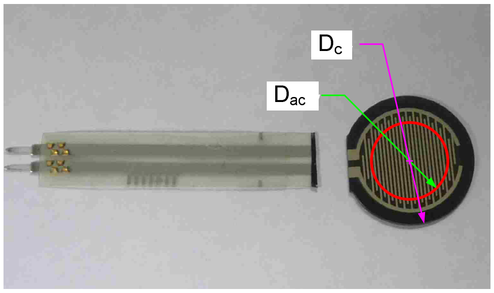

Figure 22. The Actuated Segment of FSR

Table 9. FSR 402 Mechanical Properties

Frequency (*Hz*)	**Damping *c* (*Ns/m*)**		**Stiffness *k* (*KN/m*)**	
	Test 1	Test 2	Test 1	Test 2
0.125	6.1797	6.0950	97.32	94.81
0.250	2.8768	3.0445	102.72	101.39
0.375	1.8284	1.8667	105.07	101.69
0.500	2.0041	2.0822	106.46	104.64

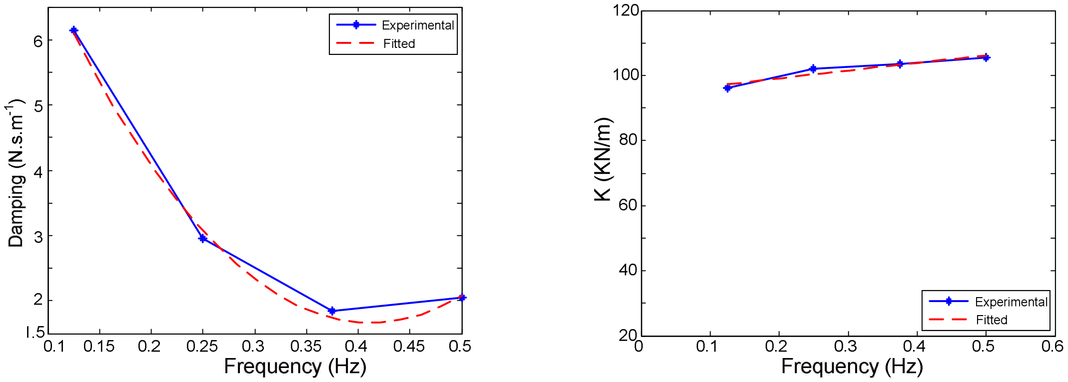

a) Damp fficient b) Me Stiffness

Figure 23. DMA Experimental vs. Fitted Data

The mathematical model shown in Figure 19 can be used to characterize the relation between the voltage of the FSR and the force applied at its surface. The relation between the input (displacement) and the output (force) is outlined in Equation 3.5.

$$F = m_{ac}\ddot{y} + c\dot{y} + ky \tag{3.5}$$

where *F* is the force applied at the FSR's surface, and *y* is the FSR's displacement.

It is assumed the FSR's voltage *V* is proportional to *y*, as follows:

$$V \propto y$$

Therefore, the relation between the *V* and *F* can be reached as in Equation 3.6.

$$F = A\left(m_{ac}\ddot{V} + c\dot{V} + kV\right) \tag{3.6}$$

where *A* is the proportionality constant.

The following performance index is used to compare the closeness of this model to the experimental results by measuring the proportion of the experimental data that can be explained by this model (goodness of fit):

$$Fitness = \left(1 - \frac{\sqrt{\sum(y_h - y)^2}}{\sqrt{\sum(y - \tilde{y})^2}}\right) * 100\% \tag{3.7}$$

where y_h is the output of the proposed model, and y represents the experimental output, with $\tilde{y}$ being the mean of the experimental output.

The experimental data were used to test the model and calibrate the A value. For this purpose, the chirp signal of Figure 19 was selected. An optimal A value of $2.258*10^{-5}$ was found using Zoutendijk's feasible direction method (Rao, 2009). Table 10 shows the fitness of the proposed system under different loading inputs.

Table 10. Second-Order Linear Model Simulation Results

Loading Input	Fitness
Chirp (0.2-20 Hz)	73.46
Square (0.20 Hz)	63.85
Square (0.10 Hz)	62.81
Step (0.1 Hz)	69.55
Triangle (0.25 Hz)	74.26
Triangle (0.10 Hz)	61.40

As shown in the table above, the proposed second-order linear model fails to satisfactorily explain the input/output relation for the loading profiles. Therefore, the possibility of obtaining a more adequate representation through the use of higher order linear and nonlinear models was investigated, as presented in the next section. Figure 24 (a-f) shows the results of the proposed model for the various input signals of Table 10.

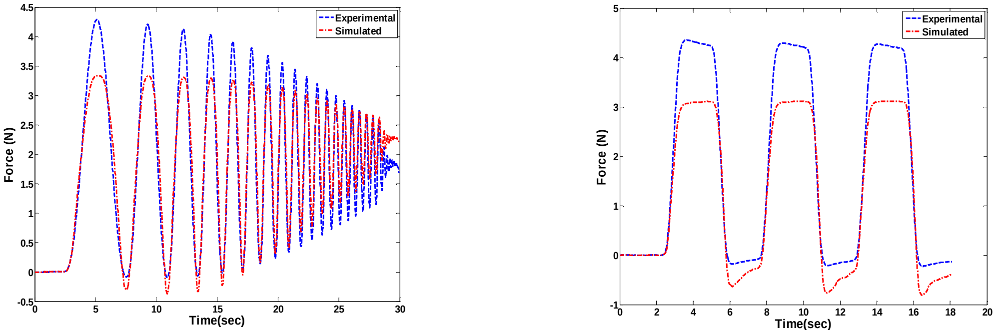

a) Chirp Input Signal

b) Square Signal (0.20 Hz)

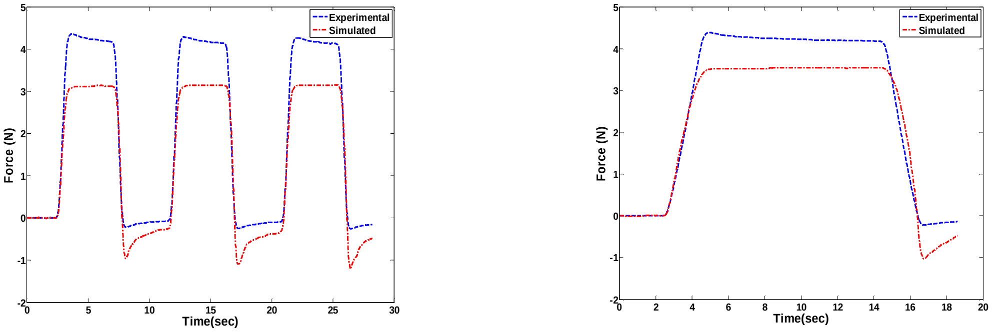

c) Square Signal (0.10 Hz)

d) Step Signal (0.10 Hz)

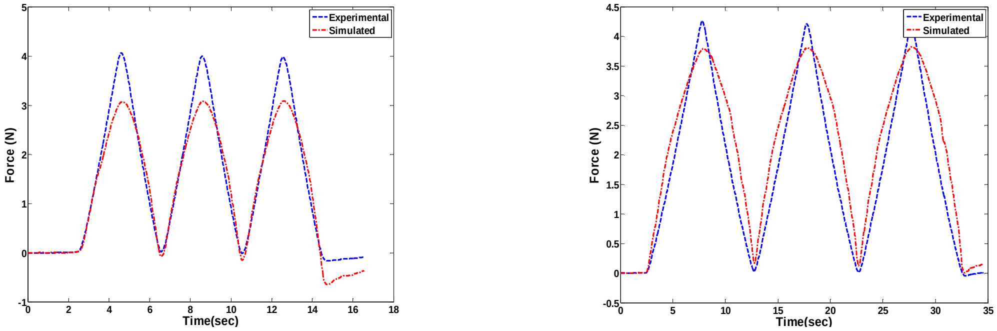

e) Triangle Signal (0.25 Hz)

f) Triangle Signal (0.10 Hz)

Figure 24. Linear System Simulation Results

Nonlinear System Identification

Nonlinear systems can be modeled as cascaded blocks of a decomposed linear along with nonlinear element(s). The model can either have a static nonlinearity at the input (Hammerstein model), a static nonlinearity at the output (Wiener model), or both input and output static nonlinearities (Hammerstein-Wiener model), as shown in Figure 25. For a detailed description about these techniques, the reader is referred to Ljung (1999).

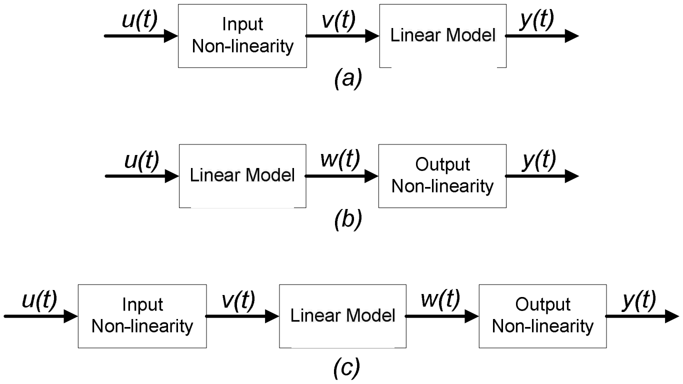

Figure 25. a) Hammerstein Model, b) Wiener Model, c) Hammerstein-Wiener Model

The Hammerstein model (Figure 25.a) can be represented by the following equations:

$$v(t) = F\big(u(t)\big) \tag{3.8}$$

$$y(t) = \frac{B(z^{-1})}{A(z^{-1})}v(t) + e(t) \tag{3.9}$$

On the other hand, the Wiener model (Figure 25.b) can be represented by the following equations:

$$w(t) = \frac{B(z^{-1})}{A(z^{-1})}u(t) + e(t) \tag{3.10}$$

$$y(t) = G\big(w(t)\big) \tag{3.11}$$

where,

$$A(z^{-1}) = 1 + a_1 z^{-1} + a_2 z^{-2} +. \dots + a_n z^{-n} \tag{3.12}$$

$$B(z^{-1}) = b_0 + b_1 z^{-1} + b_2 z^{-2} +. \dots + b_m z^{-m} \tag{3.13}$$

$$F(0) = G(0) = 0$$

$$\forall u{:}\ |F(u)| < \infty \quad \forall w{:}\ |G(w)| < \infty \tag{3.14}$$

where *u(t)* and *y(t)* are the system's input and output, respectively.

The internal signals *v(t)* and *w(t)* are non-measurable signals. The functions *F(.)* and *G(.)* can be any two functions that map the input into the output space (i.e.; polynomial, piecewise, dead zone, saturation, etc.). The nonlinear estimators are finite (Billings and Fakhouri, 1977; Giri, Chaoui, Haloua, Rochdi, & Naitali, 2002), as suggested in Equation 3.14. For instance, Equation 3.8 maps the input *u(t)* into the space of *v(t)* through the nonlinear estimator function *F(.)*. Figure 26 shows a typical piecewise linear function that maps the input into the output space. If the input/output relation involves n_k delay samples, then the first n_k coefficients of the $B(z^{-1})$ term are zeros. For detailed Wiener and Hammerstein models identification, the reader is referred to Billings and Fakhouri (1977) and Giri et al. (2002), respectively.

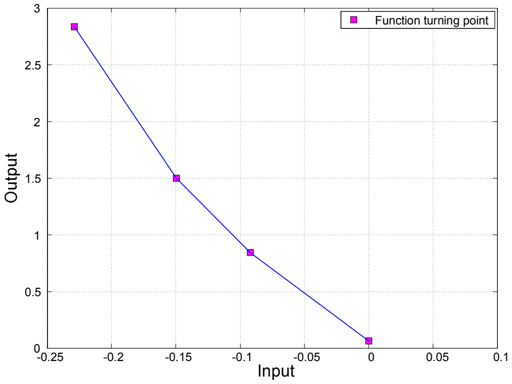

Figure 26. Piecewise Output Nonlinearity Estimator

Comparison of Linear and Nonlinear Models of the FSR

Proposed Approach

Four models of interest are developed and compared. These models are a linear model, Hammerstein, Wiener, and Hammerstein-Wiener nonlinear models. The accuracy and robustness of these four models are assessed using various loading profiles. The proposed models are created using the System Identification Toolbox of MATLAB® 2010a (Ljung, 2011).

Linear System Identification

In this work, the identification process follows these steps. First, using the chirp input signal, Figure 19, the order of the linear system was gradually increased until the results of the fitness function (Equation 3.7) couldn't be further improved significantly (Eskinat, Johnson, & Luyben, 1991). The results of this process, Table 11, are generally better than those of Table 10. These results indicate that the performances of all linear models are extremely close to each other's. The results of this section and the previous one indicate that a linear model alone is not sufficient to model the signal. Thus, it is decided to assess the effect of using linear systems in conjunction with nonlinear terms, as shown in the next section. Appendix II lists the parameters of the identified linear systems.

Table 11. Linear Model Simulation Results

Model	Linear			
Signal ↓	Linear system Order			
	2nd	3rd	4th	5th
Chirp (0.2-20 Hz)	78.79	78.85	78.92	78.93
Square (0.20 Hz)	81.86	83.12	81.89	81.89
Square (0.10 Hz)	81.93	83.28	82.12	82.10
Step (0.1 Hz)	76.25	77.87	76.62	76.59
Triangle (0.25 Hz)	76.51	77.84	76.79	76.78
Triangle (0.1 Hz)	65.52	69.17	66.14	66.09

Nonlinear System Identification

The process continues with identifying the input and output nonlinearities for the Hammerstein, Wiener, and Hammerstein-Wiener models. It is decided to use piecewise linear function breakpoints in Equations 3.8 and 3.11. Extensive testing shows that using a piecewise linear function with four breakpoints is sufficient to estimate the static nonlinearities in these three models.

Similar to the previous section, the chirp signal is used to identify the parameters of the linear and nonlinear components of the three nonlinear models. Appendices III and IV list the parameters of the identified linear parameters and the input/output pairs of the nonlinear blocks, respectively.

The fitness values for simulating different loadings using Hammerstein, Wiener, and Hammerstein-Wiener models are shown in Tables 12 through 14, respectively. As Table 12 shows, it is difficult to decide which model order results in the best results in the Hammerstein model as the best fitness values are not clustered at one order. The results of the Hammerstein model do not improve steadily with higher orders of the linear system. Table 13 demonstrates that the overall results of the Wiener model improve due to an increase in the order of the linear system. A fifth order linear system can describe more signal data than any other lesser order systems. Similar to the Hammerstein model, one cannot decide which system's order generates the best results in the Hammerstein-Wiener model, as illustrated in Table 14. In fact, the results of both the third and fifth-order linear systems are close to each other. However, the results of the Wiener model surpass all other results. Thus, the results suggest that a fifth-order Wiener model generates the best fitness values for the tested signals. This model is able to effectively describe most of the loading profiles to very satisfactory levels. Figure 27(a-f) show the results of the proposed models for various input signals.

Table 12. Hammerstein Model Simulation Results

Model	Linear			
Signal ↓	Linear system Order			
	2nd	3rd	4th	5th
Chirp (0.2-20 Hz)	90.87	95.89	91.20	91.84
Square (0.20 Hz)	85.59	79.15	83.33	86.52
Square (0.10 Hz)	89.90	90.31	87.90	90.92
Step (0.1 Hz)	83.01	83.98	86.17	81.50
Triangle (0.25 Hz)	86.69	79.40	84.96	87.47
Triangle (0.1 Hz)	65.44	43.44	69.43	63.20

Discussion of the Proposed Models

Force sensing resistors (FSRs) can be an attractive option to traditional force sensing applications, especially when the cost and space are important factors. To effectively utilize FSRs, an accurate model that can describe their behavior under different conditions is needed. This work presents a method for identifying a model for FSRs using a component characterization device.

A fixture is customized to allow proper testing of the FSR. The FSR is modeled as a second-order system where the stiffness and damping are frequency-dependent values. These values are obtained using DMA test. This linear model does not generate satisfactory results as it describes only the linear behavior of the FSR. Higher order (second through fifth) linear models are generated using system identification techniques. The same chirp signal is used as an input for all these models. The results show that increasing the order of the linear model results in minimal improvement, which lead to the conclusion that the linear models are insufficient to describe the behavior of the FSR. Both Hammerstein and Wiener models combine linear and nonlinear behaviors of the same signal. They provide simple techniques to model these nonlinearities. Three models are considered in this work: Hammerstein, Wiener, and Hammerstein-Wiener. A piecewise linear function with four breakpoints is used to model the static nonlinearities in Hammerstein, Wiener, and Hammerstein-Wiener models. It is shown that the performance of a nonlinear model is a function of several factors as; the loading profile, the order of the linear system and the nonlinear element estimator used. However, the overall performance of a Wiener model of fifth-order surpasses the other models on numerical basis.

Table 13. Wiener Model Simulation Results

Model	Linear			
Signal ↓	Linear system Order			
	2nd	3rd	4th	5th
Chirp (0.2-20 Hz)	95.23	95.47	88.96	93.46
Square (0.20 Hz)	76.98	84.16	91.50	93.02
Square (0.10 Hz)	77.67	84.52	92.67	93.52
Step (0.1 Hz)	89.54	94.84	92.82	95.01
Triangle (0.25 Hz)	78.87	85.51	91.03	92.36
Triangle (0.1 Hz)	49.82	62.08	82.02	87.25

Table 14. Hammerstein-Wiener Model Simulation Results

Model	Linear			
Signal ↓	Linear system Order			
	2nd	3rd	4th	5th
Chirp (0.2-20 Hz)	95.89	94.46	83.87	84.53
Square (0.20 Hz)	79.15	82.11	71.47	83.58
Square (0.10 Hz)	79.71	82.79	76.58	84.15
Step (0.1 Hz)	83.98	94.50	89.07	92.83
Triangle (0.25 Hz)	79.40	79.78	73.32	82.68
Triangle (0.1 Hz)	43.44	62.04	63.26	75.93

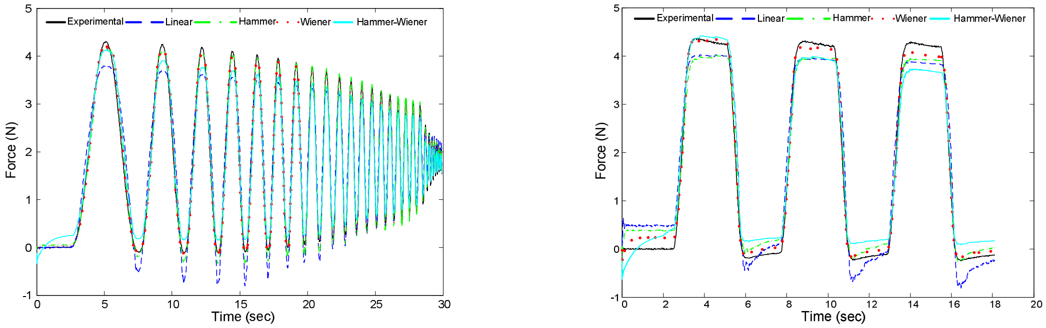

(a) Chirp Input Signal (b) Square Input Signal (0.20 Hz)

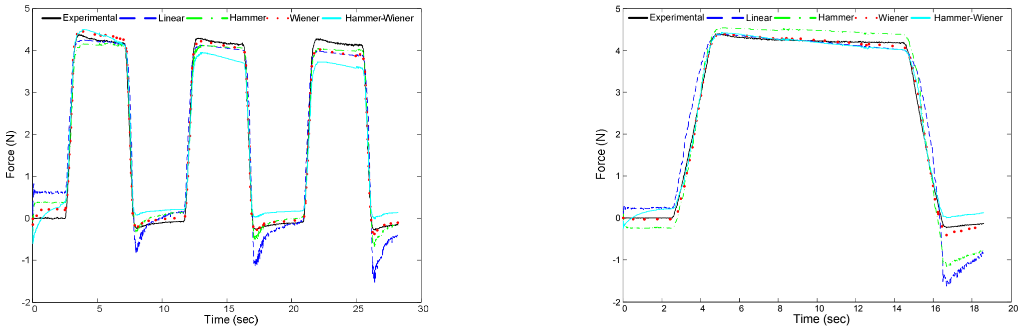

(c) Square Input Signal (0.10 Hz) (d) Step Input Signal (0.10 Hz)

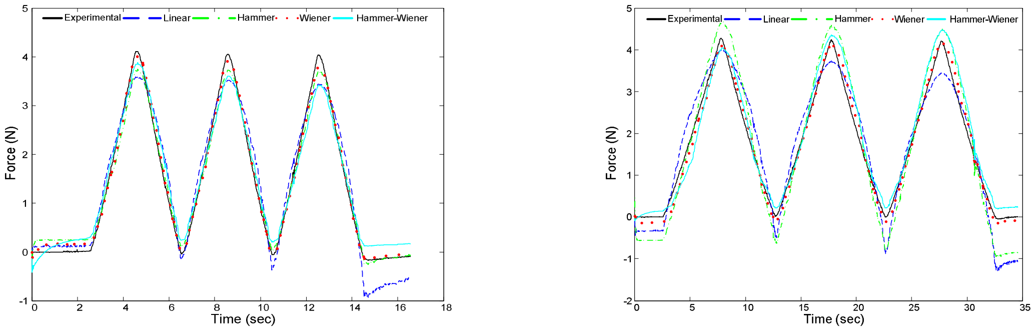

(e) Triangle Input Signal (0.25 Hz) (f) Triangle Input Signal (0.10 Hz)

Figure 27. Wiener System Simulation Results

CHAPTER 4

DESIGN OF THE FINGER-WEARABLE E-BRAILLE DEVICE

Conceptual Design of the Device

The proposed Finger-Wearable E-Braille device is a synergistic combination of mechanical and electrical components. This system is built to stimulate the touch receptors on the finger pad so that Braille characters can be comfortably read. This is done by applying adequate mechanical pressure on the finger pad through pressing the electrotactile display towards the finger pad until the required mechanical stimulation is achieved. The device is mounted on top of the distal and middle phalanges (dorsal side).

The main component of the device is the electrotactile display, which is attached to a base plate, Figure 28(a). The applied pressure on the finger pad is measured by a force sensing resistor (FSR), which is placed between the display and the base plate. Figure 28(b) shows this part of the setup. Tactile finger pad force varies between individuals. Several design options were considered, and it was finally decided to use an electric motor to generate contact force. The miniature DC motor is attached to the housing of the device. This motor lifts the electrotactile display using rack and pinion gear system. As Figure 28(c) shows, two guides are placed opposite to the two racks to ensure level motion of the electrotactile display. Figure 28(d) shows the motor and pinions, while Figures 28(e-f) show the assembled device with the shell removed and installed, respectively.

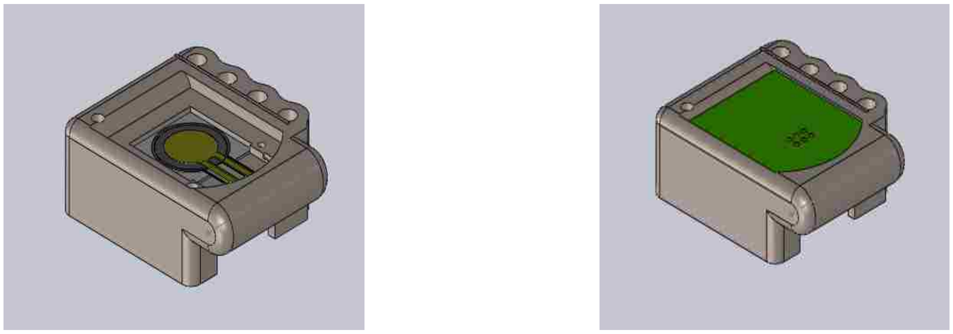

(a) FSR Installation (b) Electrotactile Board

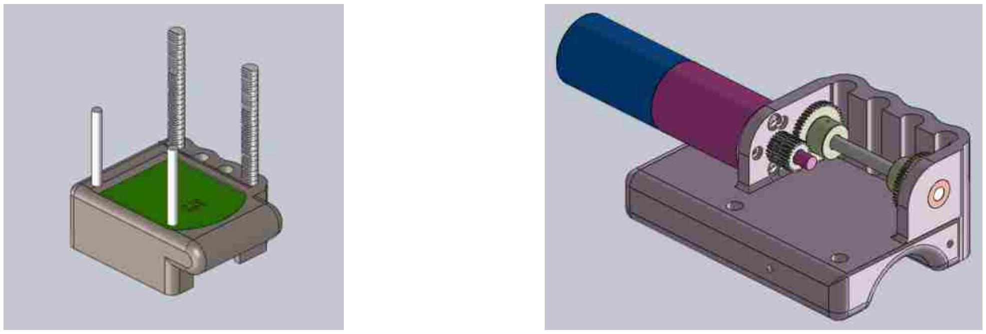

(c) E-Braille Board with Racks and Guiding Rod (d) DC Motor and Pinions

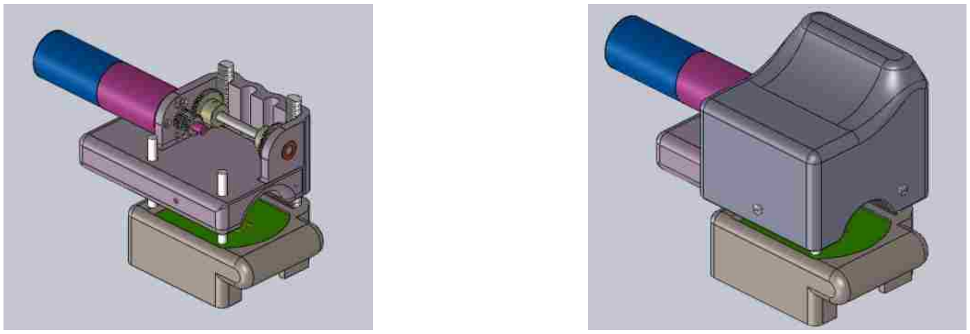

(e) Assembled Device (shell removed) (f) Assembled Device (shell installed)

Figure 28. Finger-Wearable E-Braille Model

The shell protects the mechanical components of the device and prevents any direct contact between the components and the user’s finger. The motor housing along with the base of the electrotactile display and the shell are built using a rapid prototyping machine.

Implementation of the Finger-Wearable E-Braille Device

In Chapter 2 of this study, an approach to quantify tactile force levels of human finger pads was proposed. It was found that typical tactile force threshold values range between 0.2N and 3.0N. Based on these findings, it is necessary to select a motor that is capable of generating these levels of force to maintain the electrotactile display against the finger pad. The motor should also be able to generate enough torque to account for the weight of the electronic board as well as the friction within the mechanical components. The torque produces by these forces at racks is,

$$T_{op} = (FB_{max} + W)\frac{D}{2} \tag{4.1}$$

where,

T_{op}	Output torque
FB_{max}	Maximum stimulation Braille force (3.0 *N*)
W	Weight of the base and its components (0.442 *N*)
D	Diameter of the rack pinion (13.44 *mm*)

The device uses one gear stage. The relation between the output and stall torque of the motor is,

$$T_{st} = T_{op}\left(\frac{d}{D}\right) \tag{4.2}$$

where,

T_{st}	Motor stall torque
d	Diameter of the motor pinion (6.35 *mm*)

Based on the above equations, it is found that 10.9 *N.mm* stall torque is needed. The motor selected (MicroMo Electronics Inc., 1628 024B) is a brushless DC (BLDC) motor. The motor’s stall torque is 12 *N.mm*, which makes it suitable for this application.

Additionally, a gearbox (reduction factor 43:1) is attached to the output shaft of the motor for greater output torque. This motor is small in size and light in weight (31 *gm* for the motor, 28 *gm* for the gearbox). The motor's characteristics are outlined in Table 15.

Table 15. Micromo 1628 024B BLDC Motor

Parameter		Value
Nominal Voltage	V	24 *V*
No-Load Current	I_0	52 *mA*
Rotor Inertia	J	0.54 $g.cm^2$
Terminal Inductance, phase-phase	L	525 *µH*
Terminal resistance, phase-phase	R	15.1 *Ω*
Mechanical time constant	τ	14 *ms*
Friction torque, static	C_0	0.15 *N.mm*
Friction torque, dynamic	C_v	8E-6 *N.mm/rpm*
Speed constant	k_V	1287 *rpm/V*
Back-EMF constant	k_E	0.777 *mV/rpm*
Torque constant	k_T	7.42 *N.mm/A*
Current torque	k_I	0.135 *A/N.mm*

Figure 29(a) shows how the voltage divider is placed in a dedicated cavity at the bottom of the device motor. The FSR is then attached to the voltage divider and it reaches, through a special grove, to the base plate to rest on it, as shown in Figure 29(b). The E-Braille board is fitted at the bottom of the housing, right on top of the FSR (Figure 29(c)) and it moves up and down through two racks and two guiding rods as shown in Figure 29(d). The rotary motion of the motor is translated into linear motion through rack-pinion mechanism, as illustrated in Figure 29(e). Finally, the fully assembled prototype is shown in Figures 29(f). The device is relatively light in weight and easily wearable. It can also fit most fingers' shapes.

(a) Voltage Divider

(b) FSR and Base Plate

(c) E-Braille Board with Racks and Guiding Rods

(d) Upper Part with Motor and Pinions

(e) Device Assembly

(f) Protection Cover

Figure 29. Device Prototype

CHAPTER 5

BRUSHLESS DC MOTOR CONTROLLER

BLDC Controller Design

The motion and the speed of the motor are controlled via a microcontroller board (Arduino Uno ATmega328) that interfaces a custom-built BLDC motor controller circuit. The circuit consists of three halves of an H-bridge to excite the three different phases of the BLDC motor, Figure 30.

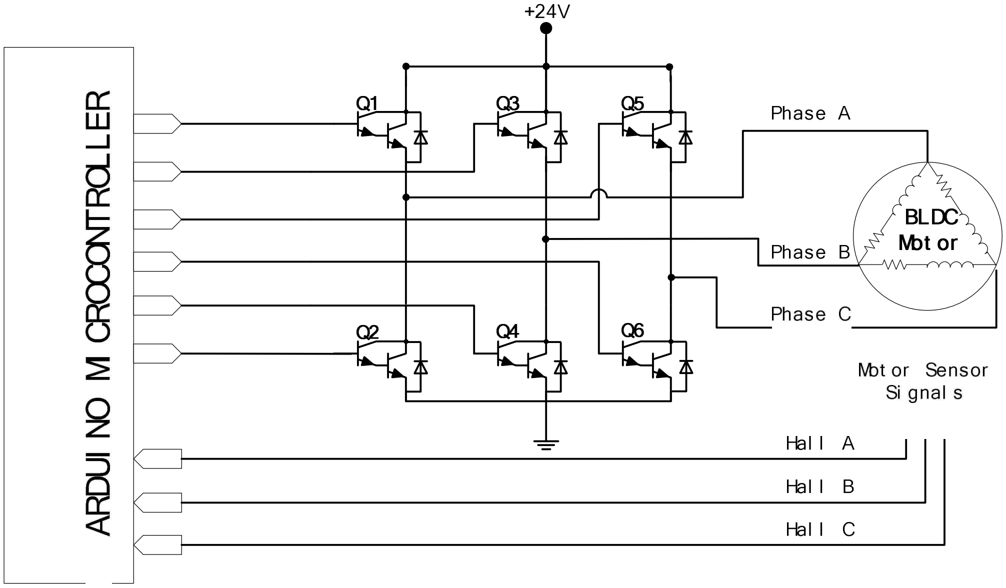

Figure 30. BLDC Motor Controller

Elements Q_1 through Q_6 are NPN Epitaxial Darlington transistors (TIP 120, 2012). The collectors of the high side of the controller (Q_1, Q_3, and Q_5) are connected to the external power supply (+24V), while the emitters of the low side of the controller (Q_2, Q_4, and Q_6) are grounded. The bases of all transistors are connected to the I/O digital pins of the Arduino board. The three signals that drive the motor (Phase A, Phase B, and Phase

C) are pulled from the connection points between the emitters of the high side and the collectors of the low side. In addition, there are six built-in fly-back diodes that are connected in parallel with the Darlington transistors to route the voltage spikes away from the controller and the circuit. These voltage spikes may generate due to the sudden change in the supply voltage through the motor inductors, as stated by Equation 5.1.

$$V = L\frac{di}{dt} \tag{5.1}$$

where L is the inductance of the motor.

The three sensor signals (Hall sensors) that come from the BLDC motor are extremely important to apply the proper commutation to generate motion. The polarity of the rotor's shaft can be identified at any point using the information from the hall sensors, and the microcontroller synchronizes the order of commutation (turning the transistors on and off) accordingly. Table 16 below shows the truth table for this BLDC motor.

Table 16. Commutation Truth Table

Hall A	**Hall B**	**Hall C**	**Motor Rotation**	**High**	**Low**
0	0	1	CW	Q_1	Q_6
0	1	0	CW	Q_5	Q_4
0	1	1	CW	Q_1	Q_4
1	0	0	CW	Q_3	Q_2
1	0	1	CW	Q_3	Q_6
1	1	0	CW	Q_5	Q_2
0	0	1	CCW	Q_5	Q_2
0	1	0	CCW	Q_3	Q_6
0	1	1	CCW	Q_3	Q_2
1	0	0	CCW	Q_1	Q_4
1	0	1	CCW	Q_5	Q_4
1	1	0	CCW	Q_1	Q_6

CW: Clock-Wise
CCW: Counter Clock-Wise

At each combination of the hall sensor inputs, the controller activates two pre-determined transistors, one from the high side and another from the low side, according to the truth table shown above. For instance, when the hall sensors read 001 and the rotation is CCW, the controller activates Q_5 and Q_2 by sending high signals at these two pins, as shown in Figure 31. The commutation of the motor continues by actuating another set of these transistors according to the hall signals shown in Table 16. Figure 32 shows the actual circuit and the interface with the microcontroller and the BLDC motor.

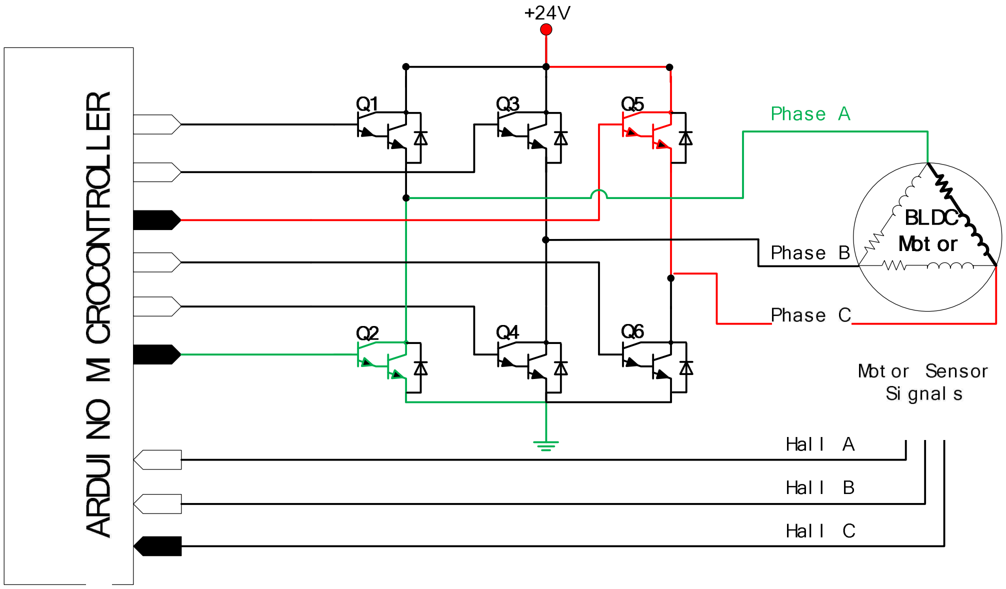

Figure 31. BLDC Motor Controller in Action

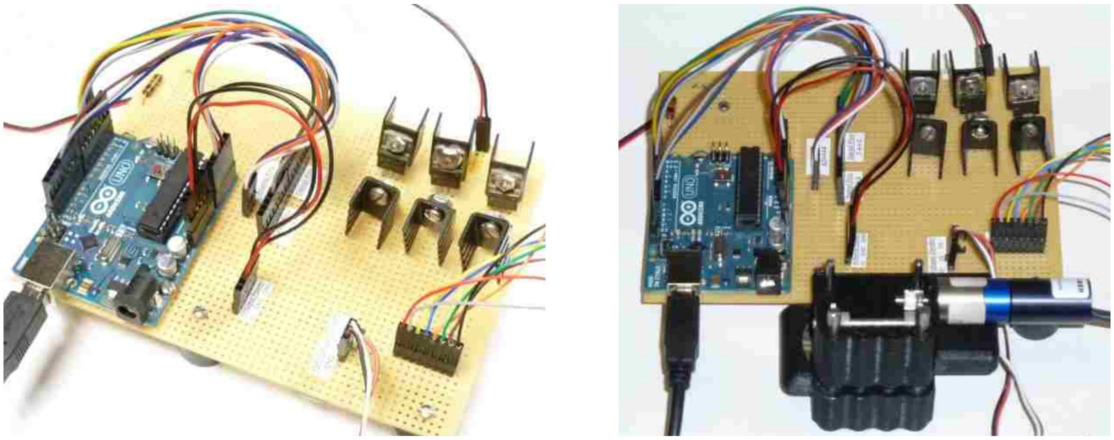

Figure 32. Components for Operating the Finger-Wearable E-Braille Device

PID Controller

One way to vary the speed of the motor is through changing the active pulse width of the driving signal, this technique is known as the pulse width modulation (PWM). PWM allows digital devices to generate analog results. This can be done by increasing or decreasing the duty cycle of the signal. That is, changing the percentage of the high level that appears in a square wave, as shown in Figure 33.

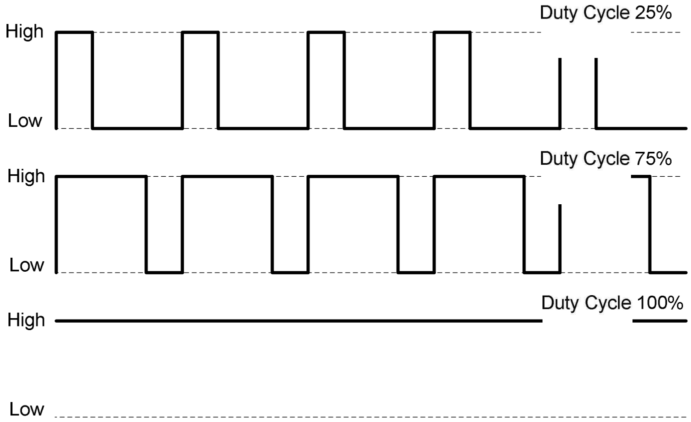

Figure 33. PWM and Duty Cycle

The ATmega328 microcontroller has six digital pins that can be programmed as PWM output pins, so a single microcontroller is sufficient to run the BLDC motor.

The full control system for this device consists of the selected controller, motor plant, rack-pinion mechanism, FSR sensor, and finally the system identification model, as illustrated in Figure 34.

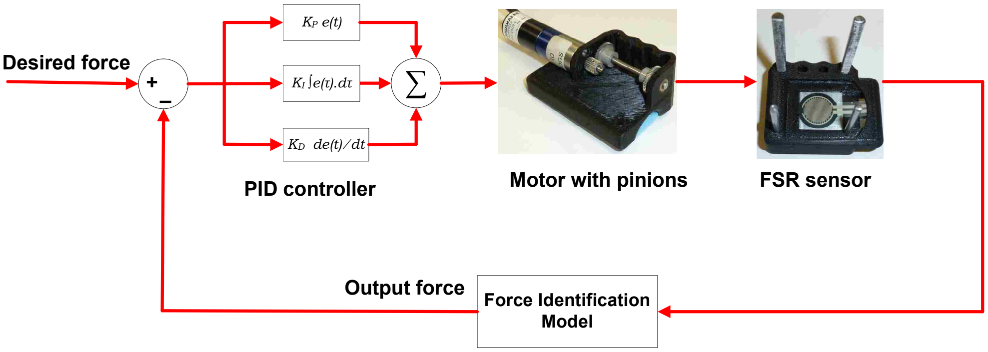

Figure 34. Control Loop

However, the FSR and the system identification model were already analyzed earlier in this study (Chapter 3) and are ready for implementation. Thus, this section will be dedicated for the design of a BLDC motor control. First, a theoretical analysis for the motor alone has been established. The FSR sensor and the system identification blocks were temporarily eliminated and replaced with a mechanical spring element of a known stiffness (K = 420 *N.m*). In this setting, the spring would resemble the existence of a finger pad while the deflection of the spring will be used as an indication for the force applied at the finger pad. This approach simplifies the theoretical and experimental analysis for the control loop by incorporating only a BLDC motor model.

A DC motor can be modeled as two sub-models that represent the armature and the rotor, as follows:

$$Rotor = {}^{1}\!/_{(J.s + Cv)} \tag{6.1}$$

$$Armature = {}^{K_t}\!/_{(L.s + R)} \tag{6.2}$$

where *J*, *Cv*, *Kt*, *L*, and *R* are defined in Table 15.

The motor uses a reduction gearhead to improve the output torque at its shaft. The gear ratio block (GR) represents the factor that transforms the motor's shaft speed into the linear velocity of the electrotactile display, as follows:

$$GR = {(\pi\, D_1\, N_1)}\big/{(60\, N_2\, RF)} \tag{6.3}$$

where:

D_1	diameter of the smaller gear (shaft gear)
N_1	number of teeth of the smaller gear
N_2	number of teeth of the bigger gear
RF	gear head reduction factor

Figure 35(a) shows the modified system's loop modeled in SIMULINK (MATLAB® 2012a, MathWorks, Inc), while Figures 35(b-c) show a human finger enclosed within the device and the spring that replaces the finger pad, respectively.

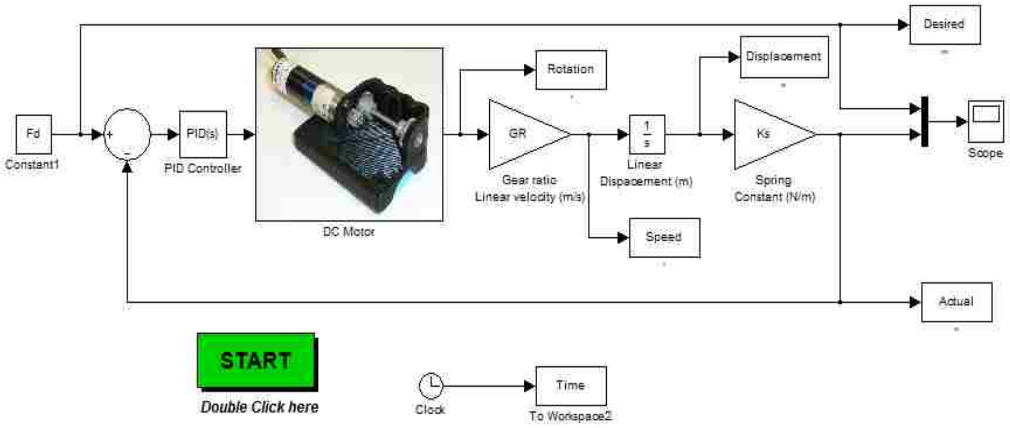

(a) Simplified System's Control Loop

(b) E-Braille Device Operating (c) A Spring Replaces Finger

Figure 35. Equivalent System Component

The response of the system, shown in Figure 36(a-b), was simulated using sisotool (MATLAB 2012a) where it indicates that the system is marginally stable as there are three simple poles that are either zeros or have negative real parts. This suggests that with increasing the gain, there is a risk that the system will fall into instability; thus, a proportional controller (P-controller) alone cannot be used. It was found that a P-controller that has a gain ($K_P > 300.39$) will drive the poles into the positive half (i.e, the response of the system will become unstable). The response of the system to a step input (3N) with $K_P = 1$ is shown in Figure 36(c).

As shown in Figure 36(c), the response of the system fluctuates around the desired value and would take relatively long time before it could settle down. However, as the gain increases, the fluctuations also increase and eventually they diverge when the system becomes unstable.

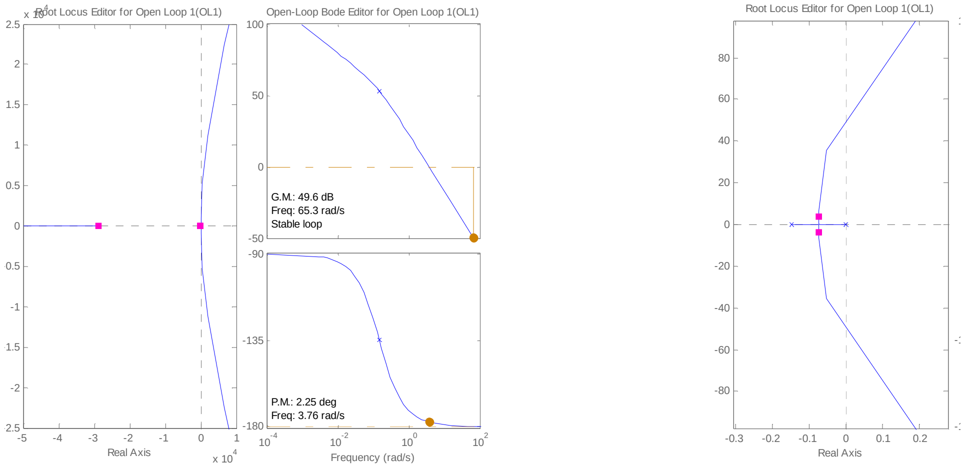

(a) Root-Locus and Bode Plot

(a) Zoom Window at Real-Imaginary Origin

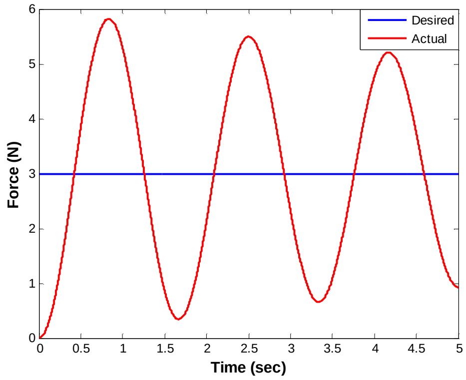

(b) Closed Loop Response of the System with a P-controller

Figure 36. Response of the System with P Compensator ($K_P = 1$)

One solution to the stability problem of this system is to add a derivative term (PD-controller). A PD-controller adds an important zero to the open loop transfer function, as follows:

$$H(s) = \frac{2.313*10^{-5}\,s + 1.157*10^{-5}}{2.835*10^{-11}.s^3 + 8.154*10^{-7}.s^3 + 1.208*10^{-7}.s} \quad (6.5)$$

The additional zero reduces the number of asymptotic branches to only two, and entices the two fundamental poles into the stability region, as shown in Figure 37(a-b).

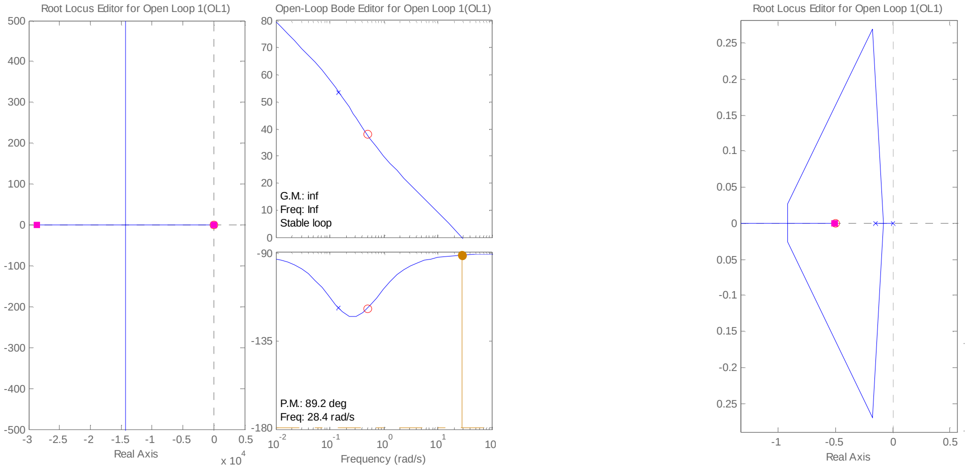

(b) Root-Locus and Bode Plot

(c) Zoom Window at Real-Imaginary Origin

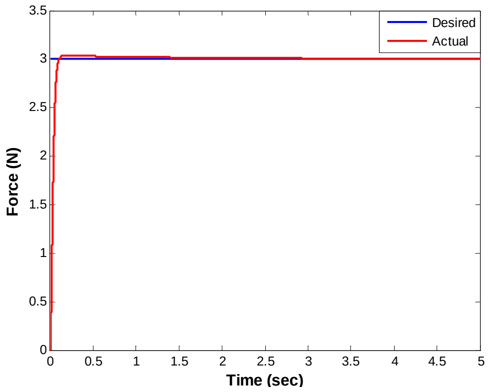

(d) Closed Loop Response of the System with a PD-controller

Figure 37. Response of the System with PD Compensator ($K_P = 1$, $K_D = 2$)

With the addition of a PD-compensator, the system became stable as increasing the gain will cause the poles to travel away from the positive half. The response of the system to the same input (3N) with $K_P = 1$ and $K_D = 2$ is shown in Figure 37(c).

Experimental Results

After identifying the FSR's response and designing the BLDC motor controller, the next step is to download all these modules into the microcontroller and validate the theoretical analysis outlined earlier. The major difficulty here is that the Arduino's low level language doesn’t support most of these advanced systems, and one needs to use other libraries to install them into the microcontroller.

An easier alternative was to use SIMULINK Coder, which allows algorithms that are built using an advanced programming language (e.g, SIMULINK) to run on the Arduino board. The SIMULINK Coder was installed on the computer; this includes some dedicated blocks that can interface with the Arduino I/O pins, as shown in Figures 38 through 42.

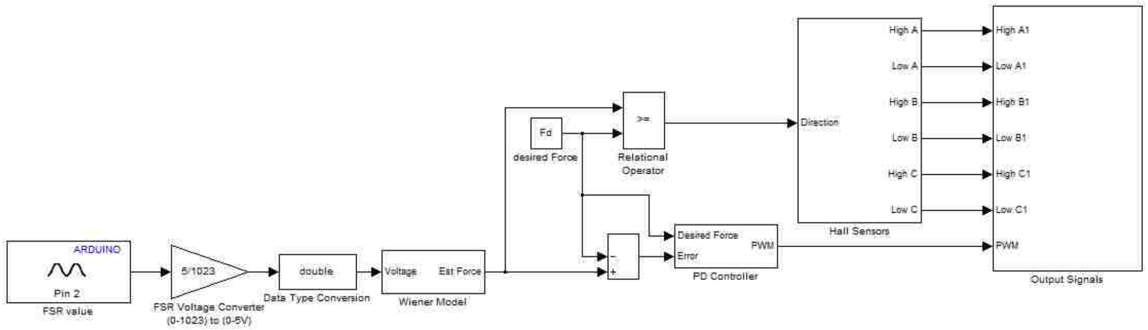

Figure 38. Overall Dynamic System

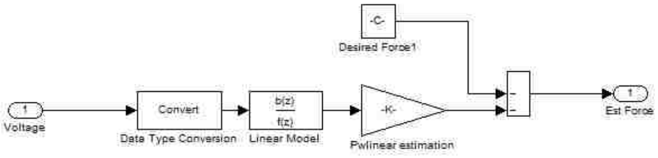

Figure 39 FSR Identification Block (Wiener Model Block)

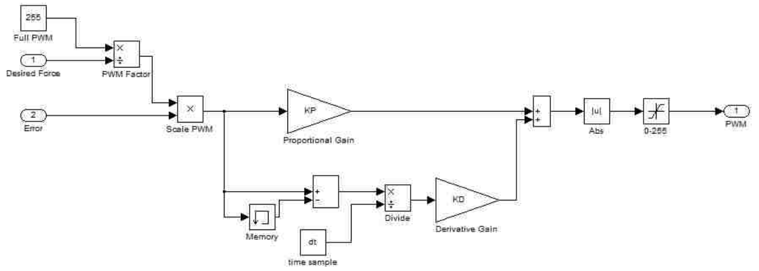

Figure 40. PD Controller and PWM (PD Controller Block)

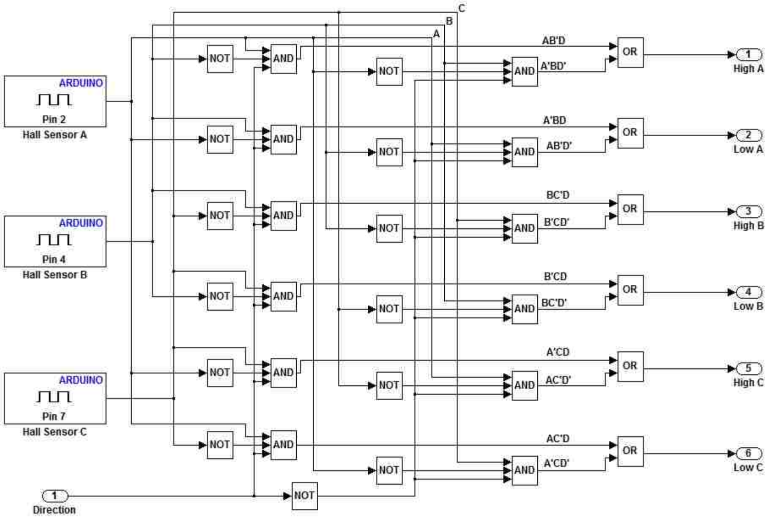

Figure 41. BLDC Commutation (Hall Sensors Block)

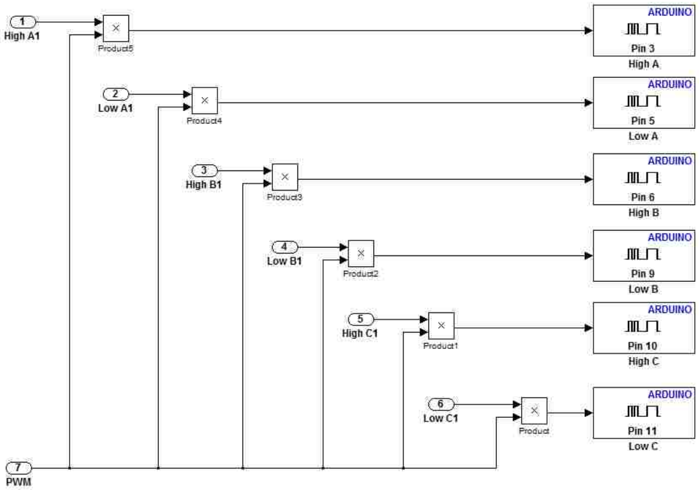

Figure 42. Interface with Arduino Pins (Output Signals Block)

Unfortunately, the microcontroller cannot be used for data logging as it doesn't have enough memory for that purpose. However, the FSR's terminals were interfaced to the computer via PhidgetInterfaceKit 8/8/8 (Phidget, 2012) and a USB cable, as illustrated in Figure 43. The FSR's digital reading (0-1000) was then mapped into (0-5V) and the voltage output was simulated using the Wiener system identification model (Chapter 3) to obtain the output force, as shown in Figure 44.

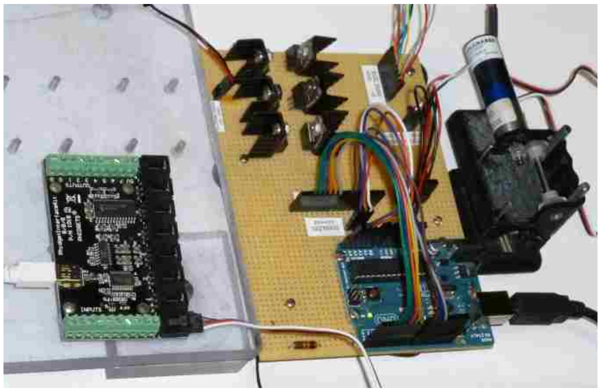

Figure 43. Phidget Data Acquisition Board

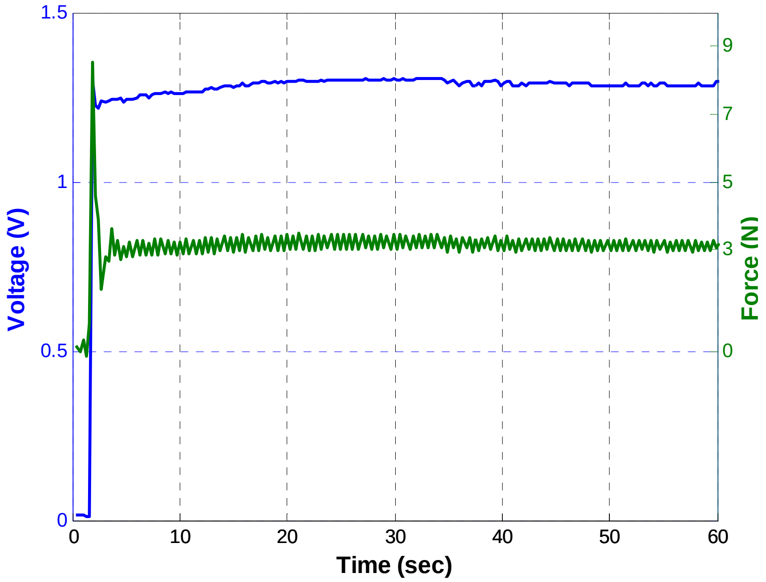

Figure 44. Real Time Voltage and Force

The FSR’s voltage in Figure 44 can be used as an indicator for the stability of the force applied at the FSR’s surface. It is shown that the device relatively regulates the force applied at the FSR’s surface. The output signal is not perfectly stable, as these disturbances may be attributed to the nonlinearities within the system components, such as; friction between racks and device housing, backlash between gears, efficiency of the electronic components, and heat dissipation of the Darlington transistors which is proven to change the transistor’s outputs characteristics.

CHAPTER 6

DISCUSSION AND CONCLUSIONS

This study aims at developing a new medical device to allow the electronic tactile stimulation of Braille characters. The study starts by quantifying the tactile forces for the human finger pad, so that the design of the device and the sensing element can be accustomed and determined accordingly. Fifty seven subjects participated in this experiment where two different tasks were designed to measure the tactile force that humans apply when identifying the dot arrangements of Braille characters. Although unfamiliar with the Braille system, a majority of the subjects were able to identify the dot arrangements for some of these characters. Quantifying the tactile forces for the human finger pad was a critical task, as the literature reviewed in this research did not agree on a standard range. In addition, two hypotheses that are related to the variation of tactile acuity with gender were tested. Results showed that there was a significant difference in finger pad area sizes between males and females. Results also indicated that within the same gender group, the forces needed to create tactile sensation through static touch were significantly higher than forces needed to induce tactile sensation during sliding. In addition, within the same gender group, the magnitude of the reaction force in the touching mode was twice the magnitude of either the reaction or the friction forces in the sliding mode.

In general, no significant difference was reported between male and female forces. An exception to that was the reaction force in the sliding experiment, which was significantly higher in males than for females. However, this difference diminished when forces were normalized into finger pad pressures. This indicated that the difference in the measured forces could be attributed to the typically smaller finger pad size of females; in that case, the finger pad forces are independent of gender. Thus, the numerical analysis of this work rejects the claim that gender is a deterministic factor in tactile acuity in favor of the claim that tactile acuity is independent of gender.

Once quantified, a force sensor that can support the measured levels of tactile forces was selected. As a passive element, the force sensor only changes its electrical resistance due to an external force that is applied at its surface. Thus, the change of the sensor's resistance can be identified with respect to the force applied at its surface such that it serves as a force sensing element. System identification techniques were used to model the force-resistance relation, and a non-linear model was able to describe this relation to a reasonable level. Force sensing resistors (FSRs) can be an attractive option to traditional force sensing applications, especially when the cost and space are important factors. To effectively utilize FSRs, an accurate model that can describe their behavior under different conditions is needed.

In this study, a method for identifying a model for FSRs using a component characterization device was presented. The FSR is modeled as a second-order system where the stiffness and damping are frequency-dependent values. These values are obtained using DMA test. This linear model does not generate satisfactory results as it describes only the linear behavior of the FSR. Higher order (second through fifth) linear models are generated using system identification techniques. The same chirp signal is used as an input for all these models. The results show that increasing the order of the linear model results in minimal improvement, which lead to the conclusion that the linear models are insufficient to describe the behavior of the FSR. Both Hammerstein and

Wiener models combine linear and nonlinear behaviors of the same signal. They provide simple techniques to model these nonlinearities. Three models are considered in this work: Hammerstein, Wiener, and Hammerstein-Wiener. A piecewise linear function with four breakpoints is used to model the static nonlinearities in Hammerstein, Wiener, and Hammerstein-Wiener models. It is shown that the performance of a nonlinear model is a function of several factors as; the loading profile, the order of the linear system and the nonlinear element estimator used. However, the overall performance of a Wiener model of fifth-order surpasses the other models on numerical basis.

The following task was to design the device while taking into account its portability and wearability requirements. A light weight design that was built in a rapid prototyping machine was introduced. The device houses the FSR sensor, the voltage divider, and the electrotactile display; it is also actuated through a miniature DC motor for additional precision. Two racks and two guiding rods were attached to the bottom part, where the racks are engaged with the two pinions on the upper part to allow the motor to lift and lower the bottom part of the device, thus allowing the physical contact to take place between the electrotactile display and the finger pad. This was followed by the selection of a DC motor that will actuate the device. A BLDC motor has many advantages over the conventional brushed motor, including: motion precision, controllability, efficient heat dissipation, lower inertia, etc. the main problem of a BLDC motor is the need for a controller circuit (motor shield) for its commutation, as it typically requires more power to run it. A controller was built using three H-bridge halves to commutate each phase of the BLDC motor independently. An Arduino Uno board that interfaces an ATmega328 microcontroller was used to synchronize the motion of the BLDC motor and to provide an I/O platform for the FSR sensor and the system calculations and conversions.

The remainder part of this work addressed the motor selection and its electrical circuitry. A brushless DC motor was selected to actuate the device. The rotational motion of the motor is transformed into a linear motion via rack-pinion mechanism. A dedicated motor controller was designed to drive the motor by using Darlington transistors to control the commutation of the motor. Finally, the control of the device is discussed briefly.

Future Expansion

This research can be extended to test other electronic components or other circuit styles, including power MOSFETs or integrated circuits (ICs). Adding more electronic components to this device will eventually result in more space occupied, while using ICs can solve this problem as they provide full line of different circuits and electronic power components all integrated within infinitesimally small and compact chips. In addition, these ICs can be easily integrated within a multilayer printed circuit board (PCB). The PCB will provide a more organized way of wiring the device, especially with including other electronic components.

The BLDC motor can also be another possible component that can be further investigated. The current motor runs on 24V power source, and it generates the torque output that is needed to operate the device. However, if another motor that requires lesser power to operate (while generating the same output torque) can be found, then this means an optimized power source and possibly some off-the-shelf battery solutions can be utilized.

The design of the device and the selection of the components were the primary objectives of this research. One other essential component has not been identified yet, namely the electrotactile display. The display has been prototyped, and the electrodes were integrated within its surface. However, there are many issues that need to be resolved, such as the physical size of the electrodes and their spatial coordination on the surface of the display. The literature in this field includes many works that have studied the discrimination thresholds of the human skin, and they can be used as a guiding tool into achieving the most appropriate electrode locations. In addition to that, the amount of current to actuate these electrodes also needs to be addressed as it will be applied directly at the human's finger pad. Finally, the controller used may not be adequate to interface all these components together. Thus, an upgrade to Arduino Mega may suffice for interfacing the electronic components, the motor, the FSR, and the electrodes.

APPENDIX I

STANDARD BRAILLE CHARACTERS

Braille characters consist of a 3x2 raised dots matrix, as shown in Figure A.1. The coding of Braille characters depends on the presence or absence of certain dots, and this makes these characters unique (a solid circle stands for a present dot and the blank stands for an absent one).

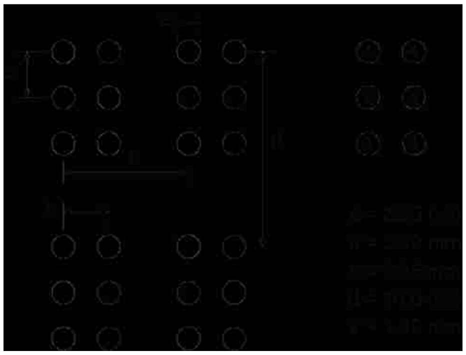

Figure A.1. Braille Characters

This coding system offers 63 different Braille characters ($2^6 - 1 = 63$), and the dots are read vertically. The dimensions between Braille character dots as well as the dimensions between adjacent characters are also shown, and the height of the dots is approximately 0.5mm (American Library of Congress).

APPENDIX II

PARAMETERS OF THE IDENTIFIED LINEAR SYSTEMS

	b_0	b_1	b_2	b_3	b_4	a_1	a_2	a_3	a_4	a_5
2nd order	5.184	-5.184				-0.001	-0.999			
3rd order	5.300	-10.546	5.246			-0.990	-0.998	0.988		
4th order	6.122	-9.867	3.963	-0.218		-0.644	-0.850	0.639	-0.145	
5th order	8.591	-20.301	19.425	-8.932	1.216	-0.543	-1.340	1.072	0.360	-0.549

APPENDIX III

PARAMETERS OF THE IDENTIFIED NONLINEAR SYSTEMS

		b_0	b_1	b_2	b_3	b_4	a_1	a_2	a_3	a_4	a_5
2nd order	**Hammer**	-1.000	1				-0.006	-0.994			
	Wiener	-1.006	1				0.005	-0.991			
	Hammer-Wiener	-1.006	1				-0.067	-0.920			
3rd order	**Hammer**	-0.503	1	-0.497			-0.990	-0.998	0.988		
	Wiener	-0.506	1	-0.494			-0.978	-0.994	0.972		
	Hammer-Wiener	-0.514	1	-0.486			-1.326	-0.249	0.576		
4th order	**Hammer**	-0.951	1	0.375	-0.423		-0.065	-1.323	0.062	0.326	
	Wiener	-0.872	1	0.166	-0.294		-0.180	-1.210	0.178	0.212	
	Hammer-Wiener	-0.341	1	-0.977	0.318		-1.938	-0.039	1.893	-0.916	
5th order	**Hammer**	-0.562	1	-0.428	0.004	-0.014	-0.479	-1.450	0.614	0.475	-0.159
	Wiener	-0.529	1	-0.631	0.339	-0.179	-0.264	-1.558	0.176	0.581	0.065
	Hammer-Wiener	-1.157	1	1.208	-0.828	-0.222	0.271	-1.848	-0.656	0.853	0.380

APPENDIX IV

INPUT/OUTPUT PAIRS OF THE NONLINEAR BLOCKS

		Input nonlinearity				**Output nonlinearity**			
		***N* pairs**				***N* pairs**			
2nd order	**Hammer**	0.143	0.479	0.833	1.150				
		-0.506	-1.776	-3.315	-5.176				
	Wiener					-0.628	-0.472	-0.301	-0.002
						3.431	2.163	1.157	0.087
	Hammer -Wiener	0.457	0.789	0.869	1.145	-1.305	-0.814	-0.577	0.103
		1.236	1.789	1.891	2.243	3.620	1.301	0.724	0.058
3rd order	**Hammer**	0.136	0.476	0.817	1.157				
		-1.192	-3.940	-6.976	-10.964				
	Wiener					-0.293	-0.189	-0.132	-0.001
						3.083	1.585	1.018	0.102
	Hammer -Wiener	-0.184	0.484	0.791	1.216	-0.049	-0.039	0.005	0.141
		-0.708	-0.049	0.139	0.316	1.507	1.288	0.761	0.063
4th order	**Hammer**	0.136	0.475	0.817	1.155				
		-0.708	-2.288	-4.116	-6.560				
	Wiener					-0.419	-0.286	-0.155	-0.020
						2.804	1.597	0.768	0.123
	Hammer -Wiener	0.139	0.505	0.788	1.158	-0.115	-0.013	0.016	0.085
		0.161	0.491	0.788	1.162	1.329	0.367	0.333	0.261
5th order	**Hammer**	0.134	0.477	0.816	1.158				
		-1.054	-3.710	-6.964	-11.386				
	Wiener					-0.229	-0.149	-0.092	0.000
						2.834	1.496	0.843	0.063
	Hammer -Wiener	0.135	0.465	0.804	1.159	-0.073	-0.053	0.001	0.042
		0.039	0.106	0.160	0.213	1.354	0.903	0.267	0.172

REFERNCES

ADA, (2010). Retrieved March 9, 2012, from http://www.ada.gov/regs2010/2010ADAStandards/2010ADAstandards.htm

American National Standard (1998), ANSI A117.1 Accessible and usable buildings and facilities. Chapter 7. Communication Elements and Features: Section 703 Signs.

Billings, S. and Fakhouri, S. (1977). Identification of Nonlinear Systems using the Wiener Model, *Electronic Letters, 13*(17), 502-504.

Birglen, L. and Gosselin, C. (1995). Fuzzy Enhanced Control of an Underactuated Finger Using Tactile and Position Sensors. Proceedings of the IEEE International Conference, Barcelona, Spain, pp.2320-2325.

Bobich, L. R., Warren, J. P., Sweeney, J. D., Helms Tillery, S. I., and Santello, M. (2007). Spatial Localization of Electrotactile stimuli on the Fingertip in Humans. *ElectrotSomatosensory And Motor Research , 24* (4), 179-188.

Bose TestBench Instruments. (2012). Retrieved March 14, 2012, from http://worldwide.bose.com/electroforce/en/assets/pdf/Products/sellsheet_TBPlanarBiaxial_022009_low.pdf

Braille Books and Pamphlets. (2005). National Library Service for the Blind and Physically Handicapped: http://www.loc.gov/nls/specs/800.pdf

Burton, H., McLaren, D. G., & Sinclair, R. J. (2006). Reading Embossed Capital Letters: An fMRI Study in Blind and Sighted Individuals. *Human Brain Mapping , 27*, 325-339.

Drewing, K., Fritschi, M., Zopf, R., Ernst, M., and Buss, M. (2005). First Evaluation of A Novel Tactile Display Exerting Shear Force via Lateral Displacement. *ACM Transactions on Applied Perception, 2* (2), 118-131

Eskinat, E., Johnson, S. and Luyben, W. (1991). Use of Hammerstein Models in Identification of Nonlinear Systems, *AIChE Journal, 37*(2), 255-267.

Fadali, M. S., Shen, Y., Jafarzadeh, S., and Yi, J. (2009). Electrotactile Preference Identification Using Fuzzy Logic, Proceedings of the 31st Annual International Conference of the IEEE Engineering in Medicine and Biology Society (EMBC'09), Minneapolis, MN

Florez, J. and Velasquez, A. (2010). Calibration of Force Sensing Resistors (FSR) For Static and Dynamic Applications. ANDESCON, 2010 IEEE, pp.1-6

Giri, F., Chaoui, F., Haloua, M., Rochdi, Y. and Naitali, A. (2002). Hammerstein Model Identification, Proceedings of the 10th Mediterranean Conference on Control and Automation - MED2002, Lisbon, Portugal.

Haase, S. J., and Kaczmarek, K. A. (2005). Electrotactile Perception of Scatterplots on the Fingertips and Abdomen. *Medical & Biological Engineering & Computing , 43*, 283-289.

Hall, R., Desmoulin, G. and Milner, T. (2008). A Technique for Conditioning and Calibrating Force-Sensing Resistors for Repeatable and Reliable Measurement of Compressive Force. Journal of Biomechanics, 41, pp.3492-3495.

Ho, V. A., Dao, D. V., Sugiyama, S., and Hirai, S. (2008). Force/Moment Sensing During Sliding Motion Using a Micro Sensor Embedded in a Soft Fingertip. 10th International Conference on Control, Automation, Robotics and Vision, (pp. 161-166). Hanoi, Vietnam.

Hollinger, A. and Wanderely, M. (2006). Evaluation of Commercial Force-Sensing Resistors. The 6th International Conference on New Interfaces for Musical Expression.

Honeywell, Model 31 Low. (2012). Retrieved March 12, 2012, from https://measurementsensors.honeywell.com/ProductDocuments/Load/Model_31_Datasheet.pdf

Interlink Electronics, FSR 402. (2012). Retrieved March 12, 2012, from http://www.interlinkelectronics.com/sites/default/files/2010-10-26-DataSheet-FSR402-Layout2.pdf

Jensen, T., Radwin, R. and Webster, J. (1991). A Conductive Polymer Sensor for Measuring External Finger Forces. *Journal of Biomechanics, 24*(9), 851-858.

Kamiyama, K., Kajimoto, H., Kawakami, N., and Tachi, S. (2004). Evaluation of a Vision-based Tactile Sensor. Proceedings of the 2004 IEEE International Conference on Robotics & Automation, New Orleans, USA, pp.1542-1547.

Kim, J.-H., Choi, W.-C., Kwon, H.-J., and Kang, D.-I. (2006). Development of Tactile Sensor with Functions of Contact Force and Thermal Sensing for Attachment to Intelligent Robot Finger Tip. IEEE Sensors, Daegu, Korea, pp.1468-1472.

Koo, I., Jung, K., Koo, J., Nam, J., Lee, Y., and Choi, H. (2006). Wearable Fingertip Tactile Display. SICE-ICASE International Joint Conference 2006. (pp. 1911-1916), Bexco, Busan, Korea.

Lebosse, C., Bayle, B., Mathelin, M. and Renaud, P. (2008). Nonlinear Modeling of Low Cost Force Sensors. IEEE International Conference on Robotics and Automation, CA, USA, pp.3437-3442

Ljung, L. (1999). System Identification: Theory for the User. Prentice Hall PTR, New Jersey, USA, Chap.5.

Ljung, L. (2011). System Identification Toolbox 7, User's Guide, MathWorks, Inc., MA, USA

Mascaro, S., and Asada, H. (2004). Measurement of Finger Posture and Three-Axis Fingertip Touch Force Using Fingernail Sensors. *IEEE Transactions On Robotics And Automation, 20* (1), 26-35

Minamizawa, K., Tojo, K., Kajimoto, H., Kawakami, N. and Tachi, S. (2006). Haptic Interface for Middle Phalanx Using Dual Motors. In Proceedings of the EuroHaptics 2006 Conference, (pp. 235-240). Paris, France.

Miyata, K., Tanaka, M., Nishizawa, T., and Chonan, S. (2006). Wearable Tactile Sensor System for Reading Braille. *International Journal of Applied Electromagnetics and Mechanics, 23,* 203-215.

Mousty, P., and Bertelson, P. (1985). A Study of Braille Reading: 1. Reading Speed as a Function of Hand Usage and Context. *The Quarterly Journal of Experimental Psychology, 37A*, 217-233.

Nakatani, M., Kawasoe, T., and Denda, M. (2011). Sex Difference in Human Fingertip Recognition of Micron-Level Randomness as Unpleasant, *International Journal of Cosmetic Science, 33*, 346-350.

Nano 17, (2012). Retrieved March 12, 2012, from http://www.ati-ia.com/products/ft/ft_models.aspx?id=Nano17

National Federation of the Blind, (2012). Retrieved March 10, 2012, from http://nfb.org/technology-resource-list

Nobels, T., Allemeersch, F., and Hameyer, K. (2004). Design of Braille cell Setting Actuators for the Application in the Braille Mouse Concept. *KIEE International Transactions on Electrical Machinery and Energy Conversion Systems , 4* (1), 12-19.

Oh, S., Cho, J., Kang, S., and Kim, E. (2006). Tactile Sensing using a Force Model of a Finger Tip. SICE-ICASE International Joint Conference, (pp. 1922-1926). Busan, Korea.

Park, K.-H., Kimt, B.-H., and Shinichi, H. (2003). Development of a Soft-fingertip and Its Modeling Based on Force Distribution. Proceedings of the 2003 IEEE International Conference on Robotics & Automation, (pp. 3169-3174). Taipei, Taiwan.

Phidget, (2012). Retrieved March 10, 2012, from http://www.phidgets.com/products.php?product_id=1018

Ramstein, C. (1996). Combining Haptic and Braille Technologies: Design Issues and Pilot Study. The Second International Conference on Assistive Technologies (ASSETS'96), (pp. 37-44). Vancouver BC, Canada.

Rao, S. (2009). Engineering Optimization: Theory and Practice, (4th ed). Wiley, NJ: Hoboken.

Sun, Y., Hollerbach, J., and Mascaro, S. (2006). Measuring Fingertip Forces by Imaging the Fingernail. Symposium on Haptic Interfaces for Virtual Environment and Teleoperator Systems, (pp.125-131). Alexandria, VA, USA.

Tanaka, M., Miyata, K., and Chonan, S. (August, 2007). A Wearable Braille Sensor System with a Post Processing. *IEEE/ASME Transactions on Mechatronics, 12*(4), 430-438

Tip 120, (2012). Retrieved March 31, 2012, from http://www.fairchildsemi.com/ds/TI/TIP120.pdf

Vaidanathan, C. and Wood, H. (1991). An Expert System Based Modeling Scheme for Tactile Data Interpretation. *Robotics and Autonomous Systems, 8*, 213-237.

Vecchi, F., Freschi, C., Micera, S., Sabatini, A., Dario, P. and Saccchetti, R. (2000). Experimental Evaluation of Two Commercial Force Sensors for Applications in Biomechanics and Motor Control. Proceedings of the 5th Annual Conference of the International Functional Electrical Stimulation Society, Aallborg, Denmark.

Voltage Divider. (2012). Retrieved March 12, 2012, from http://www.phidgets.com/products.php?category=1&product_id=1121_0

Watanabe, T., Oouchi, S., Yamaguchi, T., Shimojo, M., and Shimada, S. (2006). Development of a Measuring System of Contact Force during Braille Reading Using an Optical 6-Axis Force Sensor. Proceedings of the 28th IEEE EMBS Annual International Conference, (pp.4936-4940). New York City, USA.

Zehr, E., Stein, R., Komiyama, T. and Kenwell, Z. (1995). Linearization of Force Sensing Resistors (FSR's) for Force Measurement during Gait. IEEE-EMBC and CMBEC, Theme 7: Instrumentation, pp.1571-1572.

VITA

Graduate College
University of Nevada, Las Vegas

Mohammad Yousef Saadeh

Degrees:
Bachelor of Science, Mechatronics Engineering, 2005
University of Jordan, Jordan

Master of Science, Mechatronics Engineering, 2007
International Islamic University Malaysia, Malaysia

Special Honors and Awards:
Best Student Hardware Competition 2011 (SMASIS 2011)
Outstanding Teaching Assistant in the Department of Mechanical Engineering 2010
Best Dissertation Competition 2012 (First Place)

Publications:

Saadeh, M. & Trabia, M. (2012). Quantifying Tactile Forces in the Human Finger Pad, *Applied Ergonomics* (submitted).

Saadeh, M. & Trabia, M. (2011). Identification of a Force Sensing Resistor for Tactile Applications, *Journal of Intelligent Material Systems and Structures, JIMSS* (accepted).

Saadeh, M. & Trabia, M. (2011). Identification of a Force Sensing Resistor for Tactile Applications, Proceedings of the ASME 2011 Conference on Smart Materials, Adaptive Structures and Intelligent Systems SMASIS2011, No. 5133, Scottsdale, AZ., USA.

Saadeh, M. & Trabia, M. (2010). Development of a Measuring System of Contact Force for Braille Reading Using a Six-Axis Force Sensor, Proceedings of the 2010 International Mechanical Engineering Congress & Exposition IMECE2010, No. 39976, Vancouver, BC, Canada.

Saadeh, M., Trabia, M., Shen, Y. & Fadali, M. (2010). Design of a Wearable Haptic Braille Device, Proceedings of the 2010 Design of Medical Devices Conference DMD2010, No. 3873, Minneapolis, MN, USA.

Dissertation Title: A Refreshable and Portable E-Braille System for the Blind and Visually Impaired

Dissertation Examination Committee:
Chairperson, Mohamed Trabia, Ph. D.
Committee Member, Woosoon Yim, Ph. D.
Committee Member, Robert Boehm, Ph.D.
Committee Member, Brendan O’Toole, Ph.D.
Graduate Faculty Representative, Gabriele Wulf, Ph.D.